Cancellous bone and theropod dinosaur locomotion. Part II – A new approach to inferring posture and locomotor biomechanics in extinct tetrapod vertebrates (#22648)

First submission

Editor guidance

Please submit by **4 Feb 2018** for the benefit of the authors (and your $200 publishing discount).

Structure and Criteria
Please read the 'Structure and Criteria' page for general guidance.

Author notes
Have you read the author notes on the guidance page?

Raw data check
Review the raw data. Download from the location described by the author.

Image check
Check that figures and images have not been inappropriately manipulated.

Privacy reminder: If uploading an annotated PDF, remove identifiable information to remain anonymous.

Files
Download and review all files from the materials page.

8 Figure file(s)
4 Table file(s)

Structure and Criteria

2

Structure your review

The review form is divided into 5 sections.
Please consider these when composing your review:

1. **BASIC REPORTING**
2. **EXPERIMENTAL DESIGN**
3. **VALIDITY OF THE FINDINGS**
4. General comments
5. Confidential notes to the editor

You can also annotate this PDF and upload it as part of your review

When ready submit online.

Editorial Criteria

Use these criteria points to structure your review. The full detailed editorial criteria is on your guidance page.

BASIC REPORTING

- Clear, unambiguous, professional English language used throughout.
- Intro & background to show context. Literature well referenced & relevant.
- Structure conforms to PeerJ standards, discipline norm, or improved for clarity.
- Figures are relevant, high quality, well labelled & described.
- Raw data supplied (see PeerJ policy).

EXPERIMENTAL DESIGN

- Original primary research within Scope of the journal.
- Research question well defined, relevant & meaningful. It is stated how the research fills an identified knowledge gap.
- Rigorous investigation performed to a high technical & ethical standard.
- Methods described with sufficient detail & information to replicate.

VALIDITY OF THE FINDINGS

- Impact and novelty not assessed. Negative/inconclusive results accepted. *Meaningful* replication encouraged where rationale & benefit to literature is clearly stated.
- Data is robust, statistically sound, & controlled.
- Conclusions are well stated, linked to original research question & limited to supporting results.
- Speculation is welcome, but should be identified as such.

Standout reviewing tips

The best reviewers use these techniques

Tip	*Example*
Support criticisms with evidence from the text or from other sources	*Smith et al (J of Methodology, 2005, V3, pp 123) have shown that the analysis you use in Lines 241-250 is not the most appropriate for this situation. Please explain why you used this method.*
Give specific suggestions on how to improve the manuscript	*Your introduction needs more detail. I suggest that you improve the description at lines 57- 86 to provide more justification for your study (specifically, you should expand upon the knowledge gap being filled).*
Comment on language and grammar issues	*The English language should be improved to ensure that an international audience can clearly understand your text. Some examples where the language could be improved include lines 23, 77, 121, 128 – the current phrasing makes comprehension difficult.*
Organize by importance of the issues, and number your points	*1. Your most important issue* *2. The next most important item* *3. …* *4. The least important points*
Please provide constructive criticism, and avoid personal opinions	*I thank you for providing the raw data, however your supplemental files need more descriptive metadata identifiers to be useful to future readers. Although your results are compelling, the data analysis should be improved in the following ways: AA, BB, CC*
Comment on strengths (as well as weaknesses) of the manuscript	*I commend the authors for their extensive data set, compiled over many years of detailed fieldwork. In addition, the manuscript is clearly written in professional, unambiguous language. If there is a weakness, it is in the statistical analysis (as I have noted above) which should be improved upon before Acceptance.*

Cancellous bone and theropod dinosaur locomotion. Part II – A new approach to inferring posture and locomotor biomechanics in extinct tetrapod vertebrates

Peter Bishop Corresp., [1] , **Scott Hocknull** [1] , **Christofer Clemente** [2] , **John Hutchinson** [3] , **Rod Barrett** [4] , **David Lloyd** [4]

[1] Geosciences Program, Queensland Museum, Brisbane, Queensland, Australia

[2] School of Science and Engineering, University of the Sunshine Coast, Maroochydore, Queensland, Australia

[3] Department of comparative and Biomedical Sciences, Royal Veterinary College, Hatfield, Hertfordshire, United Kingdom

[4] School of Allied Health Sciences, Griffith University, Gold Coast, Queensland, Australia

Corresponding Author: Peter Bishop
Email address: peter.bishop@qm.qld.gov.au

This three-part series investigates the architecture of cancellous bone in the main hindlimb bones of theropod dinosaurs, and uses cancellous bone architectural patterns to infer locomotor biomechanics in extinct non-avian species. Cancellous bone is widely known to be highly sensitive to its mechanical environment, and therefore has the potential to provide insight into locomotor biomechanics in extinct tetrapod vertebrates such as dinosaurs. Here in Part II, a new biomechanical modelling approach is outlined, one which mechanistically links cancellous bone architectural patterns with three-dimensional musculoskeletal and finite element modelling of the hindlimb. In particular, the architecture of cancellous bone is used to derive a single 'characteristic posture' for a given species – one in which bone continuum-level principal stresses best align with cancellous bone fabric – and thereby clarify hindlimb locomotor biomechanics. The quasi-static approach was validated for an extant theropod, the chicken, and is shown to provide a good estimate of limb posture at around mid-stance. It also provides reasonable predictions of bone loading mechanics, especially for the proximal hindlimb, and also provides a broadly accurate assessment of muscle recruitment insofar as limb stabilization is concerned. The approach hence provides a new avenue by which to analyse, test and refine palaeobiomechanical hypotheses, not just for extinct theropods, but potentially many other extinct tetrapod groups as well.

Cancellous bone and theropod dinosaur locomotion. Part II – A new approach to inferring posture and locomotor biomechanics in extinct tetrapod vertebrates

P.J. Bishop[1,2,3,*], S.A. Hocknull[1,2,3], C.J. Clemente[4,5], J.R. Hutchinson[6], R.S. Barrett[2,3] and D.G. Lloyd[2,3].

[1]Geosciences Program, Queensland Museum, Brisbane, Queensland, Australia.
[2]School of Allied Health Sciences, Griffith University, Gold Coast, Queensland, Australia.
[3]Innovations in Health Technology, Menzies Health Institute Queensland.
[4]School of Science and Engineering, University of the Sunshine Coast, Maroochydore, Queensland, Australia.
[5]School of Biological Sciences, The University of Queensland, Brisbane, Queensland, Australia.
[6]Structure and Motion Laboratory, Department of Comparative Biomedical Sciences, Royal Veterinary College, Hatfield, Hertfordshire, UK.

*corresponding author: peter.bishop@qm.qld.gov.au.

II.1 Abstract

This three-part series investigates the architecture of cancellous bone in the main hindlimb bones of theropod dinosaurs, and uses cancellous bone architectural patterns to infer locomotor biomechanics in extinct non-avian species. Cancellous bone is widely known to be highly sensitive to its mechanical environment, and therefore has the potential to provide insight into locomotor biomechanics in extinct tetrapod vertebrates such as dinosaurs. Here in Part II, a new biomechanical modelling approach is outlined, one which mechanistically links cancellous bone architectural patterns with three-dimensional musculoskeletal and finite element modelling of the hindlimb. In particular, the architecture of cancellous bone is used to derive a single 'characteristic posture' for a given species – one in which bone continuum-level principal stresses best align with cancellous bone fabric – and thereby clarify hindlimb locomotor biomechanics. The quasi-static approach was validated for an extant theropod, the chicken, and is shown to provide a good estimate of limb posture at around mid-stance. It also provides reasonable predictions of bone loading mechanics, especially for the proximal hindlimb, and also provides a broadly accurate assessment of muscle recruitment insofar as limb stabilization is concerned. The approach hence provides a new avenue by which to analyse, test and refine palaeobiomechanical hypotheses, not just for extinct theropods, but potentially many other extinct tetrapod groups as well.

II.2 Introduction

Cancellous bone is ~~a tissue that~~ is highly sensitive and able to adapt its three-dimensional (3-D) architecture to its prevailing mechanical environment, such that the overall architecture strongly reflects the loads experienced by whole bones. ~~A multitude of experimental and theoretical studies have demonstrated that this~~ architecture can also change when loading conditions change, and that the structural alteration takes place in a predictable fashion (Adachi et al. 2001; Barak et al. 2011; Biewener et al. 1996; Goldstein et al. 1991; Guldman et al. 1997; Huiskes et al. 2000; Mullender & Huiskes 1995; Polk et al. 2008; Pontzer et al. 2006; Radin et al. 1982; Richmond et al. 2005; Ruimerman et al. 2005; van der Meulen et al. 2006; van der Meulen et al. 2009; Volpato et al. 2008; Wang et al. 2012). Furthermore, comparative studies have shown that differences in loading conditions, ~~due to~~ differences in locomotor behaviour and biomechanics, are often reflected as differences in architectural patterns between species (Amson et al. 2017; Barak et al. 2013; Fajardo & Müller 2001; Griffin et al. 2010; Hébert et al. 2012; MacLatchy & Müller 2002; Maga et al. 2006; Matarazzo 2015; Ryan & Ketcham 2002; Ryan & Ketcham 2005; Ryan & Shaw 2012; Su et al. 2013; Tsegai et al. 2013). This has also been borne out in Part I of this series, which has highlighted a number of important differences in cancellous bone architecture between the hindlimb bones of humans and birds, the two kinds of obligate, striding bipeds alive today (Bishop et al. in review-c).

As outlined in Part I of this series, the overarching paradigm that relates cancellous bone architectural fabric to its mechanical environment is the 'trajectorial theory'. First enounced by Wolff (1892), in its modern formulation ~~it~~ states that the principal material directions of a given volume of cancellous bone are aligned with the principal stress trajectories generated from physiological loading, but only at spatial scales at which cancellous bone can be treated as a continuous material (Cowin 2001). The principal material directions describe the directions in which a volume of cancellous bone is most and least stiff, whereas (continuum-level) principal stress trajectories describe how compressive and tensile forces are distributed throughout a

material under a particular loading regime. As also reviewed in Part I, ~~it has been demonstrated that~~ the principal material directions of a given volume of cancellous bone are closely aligned with its principal fabric directions, that is, the directions of strongest and weakest alignment of trabeculae (Kabel et al. 1999; Odgaard et al. 1997; Turner et al. 1990; Ulrich et al. 1999). This effectively means that the architectural fabric of cancellous bone parallels the principal stress trajectories during the normal daily use of a bone. Such a correspondence has been demonstrated to occur in a wide variety of instances, again by both experimental (Biewener et al. 1996; Lanyon 1974; Su et al. 1999) and theoretical (Beaupré et al. 1990; Carter et al. 1989; Currey 2002; Gefen & Seliktar 2004; Giddings et al. 2000; Hayes & Snyder 1981; Jacobs 2000; Jacobs et al. 1997; Koch 1917; Miller et al. 2002; Pauwels 1980; Rudman et al. 2006; Sverdlova 2011; Vander Sloten & Van der Perre 1989) studies of locomotion.

In the aforementioned theoretical studies, the general approach was the same. That is, given a continuum-level model of the bone, apply a loading regime that reflects *in vivo* physiological conditions (often derived from empirical measurements), calculate the resulting principal stress trajectories and then compare them to observations of cancellous bone architecture. It stands to reason that, if the trajectorial theory is true, the approach will also hold in reverse. Hence, it is hypothesized that, given a known whole-bone geometry and cancellous bone architecture, if one constructs a continuum-level model of the bone and seeks to determine the loading regime(s) in which principal stresses align with observed cancellous bone architecture, the resulting loading regime(s) should be physiologically realistic. It is also hypothesized that this 'reverse trajectorial approach', when framed in the context of a whole musculoskeletal system (such as a limb), should result in a physiologically realistic posture used during normal daily activity. If these predictions hold true, then this has the potential to provide new insight into understanding posture and locomotor biomechanics in extinct species, such as non-avian theropod dinosaurs, a group for which much interest surrounds their manner of locomotion (Hutchinson & Allen 2009).

The present study aimed to test the above hypotheses, and thereby investigate the validity of the reverse approach. It focused on an extant theropod species, the chicken (*Gallus gallus*), as a generalized representative for all extant, ground-dwelling birds, for which much knowledge about terrestrial locomotor biomechanics exists. By integrating musculoskeletal and finite element

modelling with observations of cancellous bone architecture, this study asked the question: "in what posture of the hindlimb do principal stresses align with observed cancellous bone architecture, and is this posture consistent with empirical observations?" In testing the reverse approach with a modern theropod and assessing its validity, the approach may then be applied to extinct, non-avian theropods, as will be done in Part III (Bishop et al. in review-b). Additionally, the results of the present study can also demonstrate how applicable this approach may be for understanding locomotor biomechanics in extinct tetrapod vertebrates in general.

II.3 Materials and Methods

II.3.1 The overall approach

The concept of using cancellous bone architectural patterns to derive *in vivo* loading regimes is not new. However, ~~the~~ approaches ~~that have been developed previously~~ (Bona et al. 2006; Campoli et al. 2012; Christen et al. 2013a; Christen et al. 2015; Christen et al. 2013b; Christen et al. 2012; Fischer et al. 1995; Zadpoor et al. 2013) are so different from that of the present study, or indeed are likely not applicable to extinct species, that an examination of these approaches will be left to the Discussion. ~~In the present study, the~~ approach of ~~identifying the~~ loading regimes and hindlimb locomotor biomechanics ~~that reflected observations of~~ cancellous bone architecture was an iterative one, which may be summarized as follows. For a given test posture, the forces and moments involved were first calculated using a musculoskeletal model, assuming a quasi-static situation, which were then transferred to a set of finite element models to calculate principal stress trajectories in the femur, tibiotarsus and fibula. These stress trajectories were then compared to the observed cancellous bone fabric in each bone, as reported in Part I of this series. The amount of correspondence between stress trajectories and cancellous bone fabric, and where this occurred, was then used to guide the set-up of a new test posture. The process was repeated until no further improvement in overall correspondence was able to be gained; at this point the 'solution posture' was achieved. Hence, in this study, a single posture is sought that best reflects as much of the observed cancellous bone architecture as possible, across all three bones.

In seeking the single posture that best reflected the architecture of cancellous bone, this study therefore sought the posture that engendered the greatest amount of remodelling stimulus in cancellous bone, to which the bones responded and adapted their architecture. Since bone remodelling is more responsive to repetitive, dynamic loading that produces greater peak strains, as well as higher strain rates (Lanyon 1996; Turner 1998), the movements in dynamic locomotion will presumably exert a strong influence on cancellous bone architecture in limb bones. It was assumed here that the loading regime at mid-stance during normal locomotion would be important for the determination of the observed cancellous bone architecture. This is because the magnitude of the ground reaction force (GRF) is substantial at around mid-stance in a wide range of animals, even if this is not when the absolute highest forces are experienced across the stance phase (Alexander 1977; Andrada et al. 2013; Bishop et al. in review-a; Blob & Biewener 2001; Bryant et al. 1987; Butcher & Blob 2008; Gosnell et al. 2011; Hutchinson 2004; Ren et al. 2010; Rubenson et al. 2011; Sheffield & Blob 2011; Witte et al. 2004). Measured *in vivo* joint reaction forces are also high at around this point in the stance (Bergmann et al. 2001; Bergmann et al. 1999; Page et al. 1993; Taylor & Walker 2001), as are the reaction forces when calculated using biomechanical models (Giarmatzis et al. 2015; Goetz et al. 2008; Lerner et al. 2015; Modenese & Phillips 2012). Hence, a general avian mid-stance posture was used as an initial starting point in the modelling process; this posture was not based on any one species, but rather represented a qualitative ‘average’ of avian postures that have been reported in the literature.

~~It is important to note that a number of~~ simplifications or assumptions were ~~made~~ throughout the modelling and simulation process. These could have been avoided or refined if only extant theropods were the ultimate focus of the study. However, as the approach outlined here needed to be applicable to extinct, non-avian theropods as well, any limitations inherent to non-avian theropods, such as absence of data concerning soft tissues (i.e., muscles, tendons, ligaments, cartilage, menisci) also had to be observed in the chicken models and simulations. Thus, when there is good evidence of a feature or constraint in both the extinct and extant species, the attempt has been made to be a specific as possible; however, when faced with considerable uncertainty or ambiguity, a more relaxed, generalized approach was taken. Not only does this tend to invoke

fewer assumptions (i.e., model simplicity), but it also enables greater consistency across species for the sake of comparison.

II.3.2 Skeletal geometry acquisition

The models developed in this study were based on a 1.56 kg adult female chicken (white leghorn breed), which was studied previously by Bishop et al. (in review-a). This specimen was different to the two specimens that were investigated in Part I, on account of logistical reasons. The intact carcass was subject to X-ray computed tomographic (CT) scanning (Siemens Somatom Definition AS+, 120 kV peak tube voltage, 255 mA tube current, 1000 ms exposure time, 0.367 mm pixel resolution, 0.2 mm slice thickness), and the resulting scans were segmented in Mimics 17.0 (Materialize NV, Belgium) via a combination of manual and automatic techniques. This produced an initial surface mesh for each bone, which was smoothed in 3-matic 9.0 (Materialize NV, Belgium), and then refined to produce a more isoparametric mesh in ReMESH 2.1 (Attene & Falcidieno 2006; http://remesh.sourceforge.net/). An isoparametric mesh is one in which the comprising triangles are all approximately equilateral in shape, and all of similar size. This is important for the generation of a volume mesh for use in finite element analyses, because the quality of the volume mesh is dependent on the quality of the surface mesh from which it is derived (Wroe et al. 2007).

Refined surface meshes were produced for the femur, tibiotarsus, fibula and tarsometatarsus (including metatarsal I), as well as the pelvis, sacrum and caudal vertebrae. These meshes were used in the creation of the musculoskeletal model and their derived volume meshes were used in the finite element model, facilitating complete none-to-node correspondence between the two modelling environments. Despite the patella and tarsal sesamoid being present in the chicken, they were not included in the development of the models, both for the sake of simplicity and also to maintain consistency with models developed for non-avian theropods (in Part III), which lack these bones. They did, however, help inform the construction of lines of action of muscles that

crossed the knee and ankle joints in the musculoskeletal model. In light of recent advances in understanding of patellar mechanics in extant birds (Allen et al. 2017; Regnault et al. 2017), future studies may be able to take the patella into account, although this would reduce comparability between models of extant birds and non-avian theropods, the latter of which lacked patellae.

II.3.3 Musculoskeletal model development

A musculoskeletal model of the right hindlimb of the chicken was constructed in NMSBuilder (Martelli et al. 2011; Valente et al. 2014) for use in OpenSim 3.0.1 (Delp et al. 2007), and is shown in Fig. 1. It comprised 12 degrees of freedom and 38 musculotendon actuators.

II.3.3.1 Definition of joints

The pelvis, sacrum and caudal vertebrae were fixed relative to each other and relative to the global reference frame, forming a single 'pelvis' segment. They were oriented such that a line through the neural canal of the anterior sacral vertebrae was horizontal and the postacetabular pelvis sloped ventrally, comparable to the orientation of the pelvis of ground-dwelling birds during stance and gait (Andrada et al. 2013; Gatesy 1999a; Rubenson et al. 2007). Although the orientation of a bird's pelvis can vary during the stride and across different speeds of locomotion (Abourachid et al. 2011; Gatesy 1999a; Rubenson et al. 2007), as a modelling simplification the position or orientation of the pelvis segment, defined by six of the 12 model degrees of freedom (three translational, three rotational), was fixed in all simulations.

The hip joint was modelled as a ball-and-socket joint with three degrees of freedom, namely flexion-extension, adduction-abduction and long-axis rotation. The three axes of rotation were initially parallel to the axes of the global coordinate system (+x is anterior, +y is medial, +z is dorsal), and the order of rotation was flexion-extension, followed by adduction-abduction, followed by long-axis rotation. The centre of the joint in the femur was determined by fitting a

sphere to the femoral head in 3-matic, and the centre of the joint in the acetabulum was determined by fitting a sphere to the concave articular surface in 3-matic. The femur was then positioned relative to the pelvis such that the joint centres of the femur and acetabulum were coincident. The 'neutral' orientation of the femur with respect to the pelvis (i.e., where all hip joint angles are zero) was such that the standard anatomical directions for the bone were set parallel to the axes of the global coordinate system (+*x* is anterior, +*y* is medial, +*z* is proximal). The neutral orientations for all bones distal to the femur were set by how they articulated with their neighbouring proximal bone.

For simplicity, the knee joint was modelled with a single degree of freedom representing flexion-extension, although it is acknowledged that in reality the avian knee is also capable of significant abduction-adduction and long-axis rotation movement (Kambic et al. 2014; Rubenson et al. 2007). No translation of the flexion-extension axis was permitted (i.e., it was fixed relative to the femur), neither was any relative movement between the tibiotarsus and fibula. The orientation and position of the flexion-extension axis relative to the femur, tibiotarsus and fibula, and the orientation and position of the tibiotarsus and fibula relative to the femur, was determined manually. This ensured that there was realistic alignment and movement of the bones across the physiological range of flexion-extension. For example, the tibiofibular crest of the lateral femoral condyle followed the space between the tibiotarsus and fibula at high flexion angles; no bone interpenetration occurred at any orientation; and the amount of space between the tibiotarsus and femur, and between the fibula and femur, remained fairly constant across the range of motion (i.e., conservation of volume of the intervening soft tissues). Additionally, the alignment of the bones was compared to their *in situ* orientations in the left and right limbs of the intact carcass, as observed from the CT scans. Asymmetry in the size and shape of the distal femoral condyles inherently meant that when the femur was in the neutral orientation, the knee joint axis was angled slightly mediolaterally in the coronal plane (Fig. 1E). Consequently, this also meant that in the neutral orientation, the distal end of the tibiotarsus and fibula were angled in towards the body midline (Fig. 1B,E).

Given the likely sizeable quantities of cartilage and menisci in the knee joint of extinct, non-avian theropods (e.g., Bonnan et al. 2010; Bonnan et al. 2013), and the fact that the present study

needed to be wholly consistent with any modelling limitations inherent to non-avian theropods, it was felt that this representation of the knee would be more reliable than a strictly objective, geometry-based definition of the joint axis (Brassey et al. 2017; Hutchinson et al. 2005; Hutchinson et al. 2008; although these studies did include space for soft tissues). This is because such a definition is only based on the available bony geometry, which may not fully reflect the actual ~~nature~~ of joint movement. Moreover, such a definition only uses half of the contributing joint surfaces, for example using the femur whilst ignoring the tibiotarsus and fibula. Differences in how the knee joint is defined would be expected to have an influence on both the orientation of the knee joint axis relative to the bones and the neutral orientation of the limb.

The ankle and metatarsophalangeal joints were both modelled with a single flexion-extension degree of freedom, although as for the knee it is acknowledged that this is a simplification of reality (Kambic et al. 2014). As for the knee joint, no translation of the flexion-extension axis was permitted in either joint; the ankle axis was fixed relative to the tibiotarsus, and the metatarsophalangeal axis was fixed relative to the tarsometatarsus. The flexion-extension axis of the ankle joint was determined in 3-matic by fitting a cylinder to the outer margins of the articular surfaces of the tibiotarsus, with the axis of the cylinder taken to be the axis of movement. The flexion-extension axis of the metatarsophalangeal joint was taken to be parallel to the *y*-axis when the limb was in a neutral orientation. Metatarsal I was fixed relative to the tarsometatarsus, and digit I was not modelled. Care was taken to ensure that bone interpenetration did not occur at these joints as well, over the range of joint motion typically reported for avian terrestrial locomotion in the literature.

The pes (digits II–IV) was modelled as a rectangular prism, parallel to the axes of the global reference frame in the neutral limb orientation, as done by Hutchinson et al. (2005, 2008). This was not only for model simplicity, but also because of the uncertainty surrounding the topology and degree of differentiation of pedal muscles in non-avian theropods (Carrano & Hutchinson 2002; Hutchinson 2002). Hence, for consistency, these modelling limitations inherent to non-avian theropods were also observed in the chicken model. The length of the prism was set as the total length of digit III, and the width set as the mediolateral width of the distal tarsometatarsus, across the condyles.

307
308
309 II.3.3.2 Definition of muscle and ligament anatomy
310
311 A total of 34 musculotendon actuators were used to represent muscles in the model; an additional
312 four actuators were used to represent the medial and lateral collateral ligaments of the knee and
313 ankle, thus allowing the possibility of 'passive' forces to be included. The origins and insertions
314 of the actuators in the model (Table 1) were derived from first-hand observations made during
315 dissections (from four individuals in total), as well as comparison to the published literature (e.g.,
316 Hudson 1937; Hudson et al. 1959; Paxton et al. 2010), and were placed as near as possible to the
317 centroid of the area of attachment in each case. The 3-D course of each actuator from origin to
318 insertion was constrained to follow anatomically realistic paths as observed during dissections
319 and reported in the literature. This was achieved through the placement of a number of
320 intermediate 'via points' (Delp et al. 1990) along the course of the actuator. Only the minimum
321 number of via points was used to achieve realistic paths, across the whole physiological range of
322 motion.
323
324 For the purposes of the current study, a number of simplifications were made regarding the
325 representation of some of the muscles:
326 1. The popliteus was not included in the model, for it runs between the proximal tibiotarsus and
327 fibula. Since relative movement between the two bones was not modelled here, inclusion of
328 the popliteus is unnecessary.
329 2. The plantaris was not included in the model, because it runs from the proximal tibiotarsus to
330 the medial aspect of the tibial cartilage surrounding the ankle; it was therefore considered
331 unlikely to play a significant role in load bearing, and thus load transmission to the bones. For
332 a similar reason, the secondary attachment of the fibularis longus (FL) to the tibial cartilage
333 was also not modelled.
334 3. On account of its small size, similar line of action to, and common insertion with, the
335 obturatorius medialis (OM), the obturatorius lateralis was not modelled: a single
336 musculotendon actuator was deemed sufficient to represent the two muscles.

4. Both parts of the flexor cruris lateralis (pars pelvica, FCLP; pars accessoria, FCLA) were modelled with separate musculotendon actuators. At the point where the FCLA diverges from the FCLP, the actuators went their own separate way towards their respective insertions, but proximal to this, they took on the same line of action towards the origin on the pelvis. A similar approach was used for modelling the two heads of the tibialis cranialis (caput femorale, TCF; caput tibiale, TCT).
5. The flexor hallucis brevis and extensor hallucis longus were not modelled, because they run from the tarsometatarsus to the ungual of digit I; as there was no degree of freedom that these two muscles could influence in the model, they were unnecessary.
6. As noted above, there is considerable uncertainty surrounding the topology and degree of differentiation of many of the digital flexor and extensor muscles in non-avian theropods (Carrano & Hutchinson 2002; Hutchinson 2002). The representation of these muscles in the chicken model was consequently simplified, to maintain consistency with non-avian theropod models, but also because the pes was modelled as a single unit. The flexor digitorum longus (FDL) and flexor hallucis longus (FHL) were modelled separately, but the deep digital flexors were represented by a single musculotendon actuator ('other digital flexors', ODF), which grossly reflected the lines of action of the individual muscles. Likewise for the extensors, the extensor digitorum longus (EDL) was modelled separately, but the deep digital extensors were represented by a single musculotendon actuator ('other digital extensors', ODE).
7. Owing to the simplified representation of the deep digital flexors, the main insertion of the FL was extended to the ventral aspect of the pes segment.

These modelling simplifications were not expected to have any significant influence on the loading conditions experienced by the femur, tibiotarsus or fibula.

The 38 musculotendon actuators so modelled here provided the forces necessary to counter collapse of the hindlimb during the simulation of a given test posture. Whilst the maximum force able to be produced by each muscle (or resisted by each ligament) could be estimated from empirical anatomical data (Calow & Alexander 1973; Hutchinson et al. 2015; Lamas et al. 2014), this is obviously not possible in the case of extinct, non-avian theropods. As such, for the sake of simplicity and consistency across extinct and extant species, all musculotendon actuators were assigned the same maximum force, 30.597 N, equal to two times body weight (BW). A value of 2

BW was chosen because some muscles would have undoubtedly been capable of exerting forces of that magnitude, or greater, as is the case in other animals (Anderson & Pandy 1999; Charles et al. 2016; Hutchinson et al. 2015; O'Neill et al. 2013; Smith et al. 2006). With all actuators having the capacity to exert forces of that magnitude, there was ample force for the actuation of each degree of freedom, obviating the need for reserve actuators (but see Section II.3.4.3 below).

II.3.3.3 Definition of segment mass properties

As a means to estimating the mass properties of each limb segment in the musculoskeletal model, the flesh surrounding each limb bone was segmented from the carcass CT scans in Mimics to produce a series of surface meshes. Using the computer-aided design software Rhinoceros 4.0 (McNeel, USA), each flesh mesh was then repositioned in space to align it with the underlying bone(s) in their neutral orientation. Additionally, the thigh segment flesh was retro-deformed to fit the pelvis and femur in the neutral pose, and care was taken to ensure that the net change in volume was negligible; this process was accomplished in Rhinoceros using the 'cage edit tool', a form of host mesh warping (Fernandez et al. 2004). The mass and centre of mass (COM) of each segment was then able to be calculated in NMSbuilder, assuming a bulk density of 1000 kg/m^3. The total mass of the right hindlimb in the model was 0.159 kg, and therefore the mass of the remaining body was 1.401 kg; this was designated as the mass of the pelvis segment in the model. Given the data reported by Allen et al. (2013), the combined COM of the whole body, minus the right leg, in their geometric model of a chicken was 0.076 m anterior to the hip joint. Scaling isometrically (via femur length) to the chicken specimen modelled here, the COM is 0.068 m anterior to the hip; this was taken to be the location of the COM of the pelvis segment in the musculoskeletal model. Since the orientation of the pelvis segment was fixed in all simulations, and all simulations were quasi-static, the only moment produced by the pelvis segment would be that by virtue of its weight, and consequently the dorsoventral position of the pelvis segment COM would not matter. As such, the dorsoventral position of the COM of the pelvis segment was assumed to be level with the hip. Moments of inertia for each segment were not calculated, on account that the simulations performed in this study were quasi-static only.

399

400 ***II.3.4 Musculoskeletal simulations***

401

402

403 II.3.4.1 Deriving a test posture

404

405 Based on the argument presented in Section II.3.1 above, a general mid-stance posture was used
406 as an initial starting posture, which was then modified in subsequent modelling iterations. It was
407 based on comparison to the kinematic data previously reported for ground-dwelling birds (e.g.,
408 Abourachid & Renous 2000; Gatesy 1999a; Grossi et al. 2014; Reilly 2000; Rubenson et al.
409 2007; Stoessel & Fischer 2012): hip extension of -30° below horizontal, hip abducted 5° from
410 midline, hip rotated 20° externally, knee flexed 93° from neutral position, ankle flexed 46° from
411 neutral position, metatarsophalangeal joint extended 16° from neutral position. The modification
412 of a given test posture to produce a new posture at the start of a new modelling iteration followed
413 hierarchical priorities: hip extension angle > knee angle > ankle and metatarsophalangeal angles,
414 with the metatarsophalangeal angle set so as to position the pes segment flat on the ground (i.e.,
415 parallel to the *x*-*z* plane). Each posture was also constrained by thee basic criteria:

416 1. No interpenetration occurred between any bones, including those of the pelvis.
417 2. The centroid of the pes segment, taken to be the location of the centre of pressure (COP) of the
418 GRF (see below), was underneath the whole-body COM in the *x*-*z* plane. This constraint
419 predominantly affected the knee, ankle and metatarsophalangeal joint angles, and was
420 necessitated by the fact that the applied ground reaction force in the simulations was vertically
421 oriented (see below).
422 3. The mediolateral step width, defined as twice the distance from the centroid of the pes
423 segment to the body midline, was less than 15% of the posture's hip height, defined as the
424 vertical distance from the hip joint centre to the base of the pes segment. This constraint
425 predominantly affected the hip adduction-abduction and long-axis rotation angles, and was
426 based on the results of Bishop et al. (2017).

427

428

429 II.3.4.2 External forces

In the present study, a given test posture was analysed as a quasi-static system. Dynamic effects such as segment accelerations were not considered, as this requires additional information and assumptions about movement, which are currently unknown for extinct, non-avian theropods. (Furthermore, incorporating dynamic effects might not actually lead to a marked change in model results, e.g., Anderson & Pandy 2001; Rankin et al. 2016.) Hence, the only acceleration in the simulation was that due to gravity, of magnitude 1 BW. In order for static equilibrium to be maintained, and also to refrain from using residual actuators of the six degrees of freedom at the pelvis, this necessitated the applied GRF to be vertical and also of magnitude 1 BW (Fig. 2). This in turn required one of the following three scenarios to also be true:

1. The centroid of the pes segment (taken as the COP of the GRF) must be directly underneath the whole-body COM, in both the *x* and *y* directions. However, the whole-body COM is on (or almost on) the body midline, meaning that in such a scenario the pes is also on the body midline. This is posturally inaccurate, because theropods employ non-zero step widths across most speeds (Bishop et al. 2017).
2. The centroid of the pes segment is not directly underneath the whole-body COM, instead having a non-zero step width. This is more posturally accurate, but static equilibrium will not be achieved unless:

(a) The COP is moved away from the centroid of the pes and retained directly under the whole-body COM. This is more speculative however, because empirical data on the path of the COP in modern bipeds shows that it remains close to the centre of the foot, not straying too far laterally or medially away from the foot midline (Schaller et al. 2011; Winter 2009).

(b) The COP is kept at the centroid of the pes, and an additional moment about the *x*-axis is applied to the pes. This moment is equal to the product of BW and the mediolateral distance between the COM and COP:

$$M_x = mg(\mathrm{COP}_y - \mathrm{COM}_y), \quad (1)$$

where m is body mass and g is the acceleration due to gravity, 9.81 m/s^2. This is physiologically implausible however, as in reality the feet can only be capable of applying a moment about the vertical (*z*) axis, the so-called ‘free moment’.

Hence, regardless of which scenario is used, some amount of accuracy must be lost in order for static equilibrium to be achieved and the simulation to be solved. The present study followed

scenario 2(b) order to maintain postural accuracy (Fig. 2). An additional moment about the *y*-axis (M_y) was also applied to the pes to account for minute positional discrepancies between the *x*-coordinates of the COP and COM (i.e., when the COP was not exactly underneath the COM), but this never amounted to more than 0.011 Nm (< 1% of the product of body weight and COM height) in any of the simulations performed.

That the applied GRF in the simulations was vertical is appropriate in the context of the current study for two reasons. Firstly, in a wide range of animals including theropods the GRF is approximately vertical, in the sagittal plane, at around mid-stance (e.g., Bishop et al. in review-a; Hutchinson 2004). Secondly, in a wide range of animals including theropods the GRF is largely vertical at the instance of peak net GRF (especially in more 'running-like' gaits), and this instance also occurs at around mid-stance (e.g., Bishop et al. in review-a). However, when the GRF is at its most vertical in the sagittal plane, or when it is at maximum magnitude, it is almost always never 1 BW in magnitude; it is sometimes a little lower, but most often it is higher, and sometimes much higher, than 1 BW. This is not a problem for the current study, because principal stress trajectories do not reflect the absolute magnitudes of applied forces, only their relative magnitudes and directions, provided that deformation remains within the elastic range (Beer et al. 2012). Moreover, in having the GRF as 1 BW in magnitude, this also facilitates size-independent comparisons across postures and across species following simulation.

II.3.4.3 Simulation and calculation of internal forces and moments

Once a test posture was established and the GRF (and associated moments) was applied, the forces developed by the musculotendon actuators to resist limb collapse were calculated in OpenSim. Although 34 muscles were represented in the musculoskeletal model, not all of them would be active and exerting force at around the mid-stance of a stride. Thus, some muscles were set to be inactive in the simulations (Fig. 2, Table 2). Which muscles were set to be inactive was determined through ~~comparison~~ to published electromyography data for birds (Gatesy 1990; Gatesy 1994; Gatesy 1999b; Jacobson & Hollyday 1982; Marsh et al. 2004; Roberts et al. 1998). Muscles that are active only in the swing phase, or active in the stance phase but only at the very

beginning or end, were considered inactive. If no data existed for a particular muscle, the following line of reasoning was employed. If the muscle belonged to the same functional group as another muscle that had been investigated (e.g., femorotibialis externus, FMTE; puboischiofemoralis lateralis, PIFL), its activity was assigned based on the recorded muscle. Failing that, if the muscle was considered unlikely to be involved in limb support at around mid-stance (e.g., ankle flexors, digital extensors, OM, IFI), it was considered inactive. If its activity still remained equivocal after that, then it was included in the model and deemed to be active, to be conservative. All four collateral ligament actuators were also included, to allow for passive forces to occur. These were modelled simply as linear 'reserve' actuators without incorporation of slack length or elasticity.

On account of the unknowable properties of muscle and ligament in extinct theropods, intrinsic force-length-velocity relationships were ignored for all musculotendon actuators in the simulations. That is, the actuators simply modelled the application of a force along a line of action set by the actuator geometry, defined in Section II.3.3.2 above. Hence, the moment M_i a given actuator exerted about a given degree of freedom i was equal to

$$M_i = a \cdot F_{\max} \cdot r_i, \quad (2)$$

where $F_{\max}$ is the maximum force capable of being produced (set at 2 BW), r_i is the moment arm of the actuator and a is the activation of the actuator, which can vary between 0 and 1. The forces developed in each musculotendon actuator were calculated using the static optimization routine of OpenSim, which solved the statically indeterminate problem of force distribution by minimizing the sum of squared activations across the actuators (Pedotti et al. 1978; Rankin et al. 2016). It was found that in no simulation did the activation of any musculotendon actuator ever approach 1; indeed, activations rarely exceeded 0.5. Coupled with the omission of intrinsic force-length-velocity relationships, this prevented nonlinearities from occurring in the static optimization routine, further facilitating size-independent comparisons across postures and across species post analysis. Due to the simplified representation of the pes segment and the muscles that cross the metatarsophalangeal joint, a reserve actuator was also applied to the metatarsophalangeal joint in the static optimization, with a maximum output set at 1,000 Nm (Fig. 2). This high value provided ample control of the metatarsophalangeal joint, and helped reduce excessively high and unrealistic recruitment of the few modelled musculotendon actuators

that crossed the joint (FDL, ODF and FL). In addition to the actual calculated forces, the line of action of all musculotendon actuators was also extracted from the posture, using the MuscleForceDirection plugin for OpenSim (van Arkel et al. 2013). Following the calculation of muscle and ligament forces, joint forces and moments were extracted using the JointReaction tool in OpenSim (Steele et al. 2012). All forces were extracted and expressed in the global coordinate system.

II.3.5 Finite element simulations

Two finite element simulations were performed for each test posture in ANSYS 17.0 (Ansys, Inc., USA), one of the femur and one of the tibiotarsus + fibula. The loads applied in these simulations were exactly the same as those calculated in the musculoskeletal simulations. Furthermore, the nodes on each bone to which muscle or ligament forces were applied in the finite element simulations were the exact same nodes to which the musculotendon actuators attached in the musculoskeletal simulations. This ensures complete correspondence between the two sets of simulations.

II.3.5.1 Geometry

The relative positions and orientations of each bone in the musculoskeletal simulations were maintained exactly in the finite element simulations. In addition to the modelling the focal bone (or bones) of interest, two extrinsic structures were created to represent the adjacent articulating bones, to more realistically model the distribution of joint forces (Fig. 3A,B). For the femur simulation, an acetabulum structure (derived from the pelvis surface mesh) and proximal crus structure (derived from the tibiotarsus and fibula surface meshes) were created. For the tibiotarsus + fibula simulation, a distal femur structure (derived from the femur surface mesh) and proximal tarsometatarsus structure (derived from the tarsometatarsus surface mesh) were created. These structures were generated simply by trimming their parent surface meshes down to the immediate area involved in the joint articulation, using a combination of Rhinoceros and 3-matic.

554 Additionally, in the proximal crus structure, the geometry was modified distally, well away from
555 the articular areas, to fuse the tibiotarsus and fibula together, limiting movement between the two
556 during the simulations.
557
558 In order to model the distribution of joint forces more realistically and evenly across opposing
559 joint surfaces, the intervening soft tissues that occur between a focal bone and its neighbouring
560 bone in life were modelled as a single volume (Fig. 3). A single, homogenous entity was chosen
561 to represent these joint soft tissues (e.g., cartilage, menisci) in the current study, as the anatomy
562 of such tissues is unknown for extinct, non-avian theropods. Moreover, this modelling
563 simplification makes the analyses more tractable for the current study, instead of involving more
564 complex, non-linear behaviours and contact formulations. The volume of soft tissues for each of
565 the hip, knee and ankle joints was produced by connecting up the closest parts of the articular
566 surfaces of the bones involved, using the 'loft' tool in Rhinoceros to create an initial mesh, which
567 was then smoothed and remeshed in 3-matic. In addition to more realistically modelling joint
568 load distribution, the approach used here also allowed for boundary conditions (restraints) to be
569 moved away from the bone (or bones) of interest, reducing the incidence of artifacts in the model
570 results (Saint-Venant's principle; Dumont et al. 2005; Gilbert et al. 2016; McHenry et al. 2007). It
571 is conceptually similar to the approach employed by Phillips and co-workers in their finite
572 element modelling of human limb bones (Geraldes et al. 2016; Geraldes & Phillips 2014; Phillips
573 et al. 2015), although the actual formulations involved are markedly different.
574
575 Volume meshes for finite element analysis were generated from the surface meshes of each bone
576 and soft tissue entity in 3-matic. All volume meshes were composed exclusively of low-order (4-
577 node) tetrahedral elements. Meshes composed of high-order (10-node) elements may produce
578 more accurate results than those composed of low-order elements, but this discrepancy decreases
579 with a greater number of elements used (Bright & Rayfield 2011; Dumont et al. 2005).
580 Furthermore, considering the relatively simple geometry of the structures being modelled here,
581 any such discrepancy was considered to be minimal. In producing the volume meshes, the
582 maximum tetrahedral edge length was constrained, so as to avoid the generation of tetrahedral
583 elements of undesirably high aspect ratios, which can lead to inaccurate results. The maximum
584 edge length for each entity was defined as being no more than double the mean edge length of the

585 triangles in the parent surface mesh. The mean edge length of the surface mesh triangles was
586 calculated as

587 $$L = \sqrt{\frac{4A}{\sqrt{3}n}}, \quad (3)$$

588 where A is the total area of the surface mesh and n is the number of comprising triangles in the
589 surface mesh. This assumes that the average triangle in the surface mesh is equilateral in shape.
590 The total number of elements used across the various postures tested ranged from 803,508 to
591 822,322 in the femur simulation and from 986,280 to 1,005,550 in the tibiotarsus + fibula
592 simulation. Although a convergence analysis was not conducted, it was considered that this was a
593 sufficient number of elements for the current study, given the relatively simple geometry of the
594 structures being modelled.
595
596 In the finite element simulations, the interfaces of adjacent contacting entities (e.g., hip soft
597 tissues and femur) were 'bonded' relative to each other, such that they did not move or separate
598 relative to each other. This facilitates seamless load transmission from one entity to another.
599 Bonded contact was also used to model the connection between the fibula and fibular crest of the
600 tibiotarsus, even though their respective interfaces were not in actual direct contact.
601
602
603
604
605 II.3.5.2 Material properties
606
607 All entities were modelled as solid, isotropic, linearly elastic materials. Three different materials
608 were defined for the entities being modelled (Table 3): bone, cartilage (for the hip and ankle soft
609 tissue entities) and a composite of the material properties of cartilage and menisci (for the knee
610 soft tissue entity). Extinct, non-avian theropods are inferred to have had menisci in their knee
611 joints, based on their widespread occurrence in extant tetrapods, including birds and crocodilians
612 (Chadwick et al. 2014; Haines 1942; Wink et al. 1989; Zinoviev 2010), but the actual
613 morphology of these menisci remains speculative. This is one of the reasons for modelling all
614 soft tissues in the knee joint as a single, homogenous entity, in addition to being a computational

simplification. The material properties assigned for bone were conservatively estimated from the most common values reported for cortical bone in the literature (e.g., Currey 2002, and references cited therein; Erickson et al. 2002; Reed & Brown 2001). The material properties for cartilage and menisci were also conservative estimates, derived from the literature (e.g., Currey 2002, and references cited therein; Kazemi et al. 2013; Stops et al. 2012).

In previous finite element studies, cartilage and menisci have been represented with a variety of material behaviours, including isotropic and transversely isotropic linear elasticity, hyperelasticity, viscoelasticity and poroelasticity (Kazemi et al. 2013; Stops et al. 2012). The use of isotropic, linearly elastic material behaviour in the present study is justified on the following grounds. Firstly, as the analyses of the present study were quasi-static ~~in nature~~, the time (strain rate) dependency of nonlinear material properties can be ignored with minimal error (Carey et al. 2014). Secondly, the precise kind of material behaviour, or material properties, is virtually unknown for any archosaur (extinct or extant). Thirdly, assuming an isotropic, linearly elastic material behaviour kept the model simple and minimally speculative, and also reduced the computational cost of solving the finite element models.

A solid, isotropic, linearly elastic continuum representation was also necessitated for the bone entities in the simulations. Not only is this ~~due to the fact that~~ material properties (and any anisotropy thereof) are unable to be determined for extinct theropods, but moreover anything other than this representation could compromise the objectives of the current study. Specifically, the introduction of any sort of structural or material heterogeneity, discontinuity or directionality will influence the resulting principal stress trajectories. Since a key objective of this study was to examine the ~~nature~~ of the calculated principal stress trajectories~~,~~ in relation to cancellous bone architecture, directionality needed to be a model output only, not a model input.

II.3.5.3 Loads and restraints

For each simulation, four sets of loads were applied: muscle and ligament forces, joint forces, joint moments and segment weight. As noted above, muscle and ligament forces were applied to

the same nodes as were involved in the musculoskeletal simulations. Additionally, a given muscle or ligament force was evenly spread out over a number of nodes (generally around 20), centred about the focal node, in order to reduce the incidence of artifacts in the model results.

Joint forces were applied to a focal bone via its neighbouring bones. Here, one neighbouring bone was restrained in translation in all three axes, whilst the other was used to apply a joint force; the joint force at the restrained end of the bone was provided by the reaction at the restraints, transmitted back through the bone of interest. In both the femur and tibiotarsus + fibula simulations, the knee joint force was applied directly via the appropriate neighbouring bone (proximal tibiotarsus + fibula and distal femur, respectively), with the other neighbouring bone being restrained (acetabulum and proximal tarsometatarsus, respectively). In ANSYS, this approach was implemented by using a 'remote force' (Fig. 3D). This is where a force is applied to a specific entity, but via a remote point in space that is topologically attached ('scoped') to the entity; when a force is applied to the remote point, the target entity gets pulled or pushed along with it, along the line of action of the applied force. In ANSYS, this is accomplished by a set of constraint equations that relate the degrees of freedom of an entity's nodes to the remote point; one constraint equation exists for each node in the entity experiencing the remote force. The location of the remote point in both the femur and tibiotarsus + fibula simulations was specified as the location of the knee joint centre in the musculoskeletal model. This meant that the joint force was applied properly, without introducing any moments into the system, because the net force vector passed through the correct location in space, again ensuring complete correspondence between the finite element and musculoskeletal simulations.

The knee joint moment was applied directly to the appropriate bone or bones, by applying it to the surface or surfaces in contact with the knee soft tissues; for example, by applying it to the distal femur in the femur simulation. This direct application was chosen, as opposed to the moment being applied via a neighbouring bone, because the greater compliance of the knee soft tissues would not allow full transmission of the moment to the bone or bones of interest. No hip joint moment was involved, since the hip joint was modelled as a ball-and-socket joint, and thus unable to resist moments. Whilst an ankle joint moment was calculated in the musculoskeletal simulations, it was not able to applied in the tibiotarsus + fibula finite element simulations. This

is because of the close proximity of the ankle end of the tibiotarsus to the restraint, and thus the restraint would greatly alter the transmission of any applied moment; this modelling deficiency will be returned to in the Discussion (Section II.5.1).

The weight of the appropriate segment (e.g., thigh segment weight in the femur simulation) was applied via a remote point that was scoped to the entire bone of interest. The location of the remote point was set as the COM of the limb segment.

II.3.5.4 Model solution

All finite element simulations were solved as linear static systems in the Static Structural module of ANSYS. Additionally, all simulations used inertia relief, which is a technique that is used to counter unbalanced forces, so as to produce no net acceleration of the model (Liao 2011). This is achieved through the application of an inertial force and moment to the model's centre. Although the musculoskeletal simulations described above were analysed under the assumption of static equilibrium, this does not exactly occur in finite element simulations due to non-rigid behaviour of the various entities. In particular, the soft tissue structures are highly compliant relative to the bone structures, and deformation of these soft tissue structures during simulation will lead to an imbalance of the applied forces. This has the potential to produce a positive-feedback loop where force imbalance leads to model acceleration, which leads to further deformation, which in turn leads to greater force imbalance, and so on. Ultimately, very large and unrealistic deformations occur, and calculated model results are unreliable. Thus, inertia relief was used to counter the initially very small imbalance in forces that results upon deformation of the model; for instance, in the femur simulation of the solution posture, the applied inertial force was

$$(F_x, F_y, F_z) = (7.1725 \times 10^{-8}, 6.7934 \times 10^{-8}, -1.1303 \times 10^{-6}) \text{ N},$$

and the applied inertial moment was

$$(M_x, M_y, M_z) = (1.7224 \times 10^{-6}, 3.3496 \times 10^{-6}, -5.3604 \times 10^{-7}) \text{ Nm}.$$

The very small magnitude of these adjustments justifies the use of this technique in the current study.

II.3.6 Results analysis

Upon performing the finite element simulations for a given test posture, the calculated stress tensor at each node in each bone entity was exported from ANSYS. A custom script in MATLAB 8.0 (MathWorks, USA) was then used to perform an eigenanalysis of the stress tensor data, producing the vector orientations of the principal stresses. Their 3-D trajectories were then visualized using this MATLAB script, as well as Rhinoceros. These trajectories, particularly of the maximum principal stress ($\boldsymbol{\sigma}_1$, usually signifying tension) and minimum principal stress ($\boldsymbol{\sigma}_3$, signifying compression) were visually compared to the architectural patterns of cancellous bone fabric reported for birds in Part I (Bishop et al. in review-c). As a further aid to assessing the degree of correspondence between principal stresses and cancellous bone fabric, the direction of $\boldsymbol{\sigma}_3$ in the femoral head and medial femoral condyle was quantitatively compared to the mean directions of the primary fabric direction ($\mathbf{u}_1$) for those parts of the femur in birds, also as reported in Part I. As $\boldsymbol{\sigma}_3$ is compressive, it stands to reason that this will show the greatest correspondence with the architecture in the femoral head and medial femoral condyle, both of which would be expected to be exposed predominantly to compressive joint loading. The direction of $\boldsymbol{\sigma}_3$ in the femoral head was taken to be the mean direction of vectors in the region of a sphere of radius one-half of that fit to the entire femoral head (performed in 3-matic), and positioned just under the surface of the bone, underneath where the hip force was received in the finite element simulations. The direction of $\boldsymbol{\sigma}_3$ in the medial femoral condyle was taken to be the mean direction of vectors in the region of a sphere of radius one-third of that fit to the condyle (performed in 3-matic), and positioned in the anatomical centre of the condyle. Higher priority was given towards improving correspondence in the femoral head over the medial condyle, since hip angles are presumed to be more important for determining overall posture in bipeds. Additionally, strict comparison between the mean directions of $\boldsymbol{\sigma}_3$ and $\mathbf{u}_1$ in the medial femoral condyle ignores the 'fanning' of $\mathbf{u}_1$ that occurs in this region of the bone (see Part I), and hence is less legitimate.

Comparisons were made from the chicken finite element stress results to the architectural patterns observed in ground-dwelling birds as a whole for two main reasons. Firstly, it has been shown that birds as a whole appear to demonstrate a largely consistent pattern of cancellous bone

architecture in the femur, tibiotarsus and fibula (Part I). Secondly, cancellous bone architecture was not able to be extensively quantified in smaller birds such as chickens, owing to continuum level restrictions (relatively few trabeculae; see Part I). Due to the small sample size for each avian species examined thus far (Part I), and given the exploratory nature of the present study, it is prudent (and conservative) to make comparisons to ground-dwelling birds as a whole, until such a time as it can be demonstrated that there exist significant interspecific differences, in terms of both locomotor behaviour and cancellous bone architecture.

II.3.7 Caveats

Two points are worth noting about the overarching philosophy of the approach of the current study. Firstly, this study sought to determine a *single posture*, the principal stress trajectories of which showed the greatest degree of correspondence to observed cancellous bone architecture in the femur, tibiotarsus and fibula. Cancellous bone, however, experiences many different loading regimes throughout the course of normal daily activity, each of which engenders a remodelling stimulus, and to which cancellous bone responds and adapts its architecture (Kivell 2016). This has been demonstrated in many previous computational theoretical studies, whereby no one loading regime will lead to replication of all of the observed architectural features in a bone; only when multiple loading regimes are considered can all of a bone's cancellous architecture be explained (Beaupré et al. 1990; Bona et al. 2006; Boyle & Kim 2011; Carter & Beaupré 2001; Carter et al. 1989; Coelho et al. 2009; Jacobs et al. 1997; Jang & Kim 2008; Jang & Kim 2010a; Jang & Kim 2010b; Phillips et al. 2015; Sverdlova 2011; Tsubota et al. 2002; Tsubota et al. 2009; Turner et al. 1997). Therefore, in seeking a single posture that best reflects the observed cancellous bone architecture, the current study in fact searched for a 'characteristic posture', which is a time- and load-averaged posture across all loading regimes. This characteristic posture may or may not be an actual posture used at a particular instance in a particular behaviour. As argued above, however, the posture at around the mid-stance of a stride will probably be important, and the characteristic posture so derived may therefore bear considerable resemblance to it.

Secondly, ~~it is acutely obvious that a great~~ many assumptions and modelling simplifications ~~were made~~ in this study. Many of these were necessitated by the lack of empirical data for extinct, non-avian theropods, such as soft tissue anatomy or material properties, which in all likelihood will never be obtained. Other simplifications pertained to making the system more tractable for analysis and interpretation, such as representing the knee and ankle joints with a single degree of freedom each, when it is known that these joints are capable of more complex motions during locomotion in birds (Kambic et al. 2014; Rubenson et al. 2007). All of the assumptions and simplifications involved in the present study could in principle be investigated via sensitivity analysis, but no such analysis was performed here, save for one aspect (see next section below). Instead, all assumptions were kept at their 'best guess' manifestation throughout the study. By keeping every aspect of every stage of the modelling process constant, and only varying posture, this allowed for the direct comparison of simulation results to postural differences: differences in model results were entirely due to differences in limb posture. When these assumptions are also held constant in a comparative context across species (Bright 2014), this also allows for a more direct assessment of the effects of posture on limb bone loading and muscular recruitment (Part III).

II.3.8 Sensitivity to muscle forces

In the musculoskeletal simulations, all musculotendon actuators were assigned the same maximum force (2 BW) for the sake of simplicity and also to facilitate consistency across extinct and extant theropod species. In reality, the varying sizes and architectures of the different muscles mean that they can have greatly different maximal force capabilities, which may have an important effect on the end results. To examine how sensitive the results were to using more realistic muscle force capabilities, the solution posture identified above was re-analysed with muscle-specific maximum force capacities stipulated. The original chicken carcass used to build the model was not able to be dissected for measurement of muscle architecture, and so the data collected by Paxton et al. (2010) for an adult (2.08 kg) junglefowl were used instead, scaled to the chicken model in proportion to mass. Maximum muscle force for each of the active muscles was then calculated following standard formulae, assuming a constant isometric stress of 3×10^5

N/m^2 (Medler 2002); values are reported in Table 4. The maximum force for the four collateral ligaments modelled was left unaltered from the original values.

The results for both the musculoskeletal and finite element simulations of this sensitivity test are reported below alongside those for the main simulations.

II.4 Results

A total of eight different postures were tested before no ~~further~~ correspondence between principal stress trajectories and cancellous bone architectural patterns ~~was able to be~~ achieved (Fig. 4A). Going from the worst to best postures tested, the angular deviation between the minimum principal stress ($\boldsymbol{\sigma}_3$) and the primary fabric orientation ($\mathbf{u}_1$) in the femoral head decreased from 23.3° to 7.9°, a 66% reduction; likewise, the angular deviation between $\boldsymbol{\sigma}_3$ and $\mathbf{u}_1$ in the medial femoral condyle decreased from 29.2° to 17.3°, a 41% reduction. The final solution posture is illustrated in Fig. 4B–C. The 'degree of crouch' (Bishop et al. in review-a) of this posture is 0.160; the degree of crouch in a standing posture, as empirically predicted from the total leg length of the chicken individual modelled (275 mm), would be 0.166 (Bishop et al. in review-a). It is worth remembering that despite this close similarity, the solution posture should not be equated literally with any single real posture used (be it of standing, slow walking, fast running, etc.), for it is a characteristic weighted average of all postures used.

II.4.1 Principal stress trajectories

In the solution posture, the principal stress trajectories in the femur, in particular those of $\boldsymbol{\sigma}_3$ (compressive), showed a high degree of correspondence with the observed cancellous bone architectural directions, in the femoral head, under the facies antitrochanterica, in the trochanteric crest and in both femoral condyles (Fig. 5A–H). The mean direction of $\boldsymbol{\sigma}_3$ in the femoral head

showed strong correspondence to the mean direction of $\mathbf{u}_1$ measured for birds (Fig. 5I). Fair correspondence between $\boldsymbol{\sigma}_3$ and $\mathbf{u}_1$ also occurred in the medial femoral condyle, although the direction of $\boldsymbol{\sigma}_3$ was notably more posteriorly inclined than the mean direction of $\mathbf{u}_1$ across all birds (Fig. 5J); a more posteriorly inclined orientation of $\boldsymbol{\sigma}_3$ occurred in all postures tested.

Much correspondence between principal stress trajectories and cancellous bone architecture was also observed in the tibiotarsus, particularly in the proximal end (Fig. 6). In the anterior cnemial crest, the trajectory of the maximum principal stress ($\boldsymbol{\sigma}_1$, tensile) largely paralleled the margins of the crest, as observed for cancellous bone fabric. In much of the lateral cnemial crest, the observed cancellous bone fabric reported for birds was reflected by the trajectory of $\boldsymbol{\sigma}_3$. Under the articular facies, the trajectory of $\boldsymbol{\sigma}_3$ corresponded closely with the observed architectural patterns there, showing a posterior inclination largely parallel to the sagittal plane. Additionally, in the sagittal plane through the middle of the proximal end, $\boldsymbol{\sigma}_1$ and $\boldsymbol{\sigma}_3$ formed a double-arcuate pattern, closely resembling a similar pattern in $\mathbf{u}_1$ observed in some of the large bird individuals studied in Part I (Fig. 6K). In contrast to the proximal tibiotarsus, only minimal correspondence between principal stress trajectories and cancellous bone architecture could be attained in the distal tibiotarsus, in any posture tested. In the solution posture, there was some correspondence between $\boldsymbol{\sigma}_3$ and observed architecture in the immediate vicinity of the articular condyles, where $\boldsymbol{\sigma}_3$ was largely parallel to the sagittal plane (Fig. 6L), but this was not observed throughout the entire distal end of the bone, unlike the architecture.

The principal stress trajectories in the fibular head showed strong correspondence to the gentle inclination observed in the cancellous bone architecture (Fig. 7). Medially, $\boldsymbol{\sigma}_1$ showed this pattern, whereas laterally, it was $\boldsymbol{\sigma}_3$ that showed this pattern.

II.4.2 Mid-shaft stresses

In the solution posture, the most axis-parallel orientation of both $\boldsymbol{\sigma}_1$ and $\boldsymbol{\sigma}_3$ at the femoral mid-shaft was at a high angle to the long-axis of the bone, by at least 30°, indicating considerable torsion (Fig. 8A). Moreover, the sense of torsion as indicated by the stress trajectories was

positive; when the right femur is viewed proximally, the proximal end was rotated counterclockwise relative to the distal end (Fig. 8B). The neutral axis of bending was oriented 36° from the mediolateral axis, indicating that bending of the femur was predominantly in an anteroposterior direction.

In the tibial mid-shaft, the most axis-parallel orientation of $\boldsymbol{\sigma}_1$ and $\boldsymbol{\sigma}_3$ was almost parallel to the long-axis of the bone, indicating only a minimal torsion (Fig. 8C). The sense of torsion (what very little there is) as indicated by the stress trajectories was also positive. The neutral axis of bending was oriented 19° from the mediolateral axis, indicating that bending of the tibiotarsus was also in a predominantly anteroposterior direction.

II.4.3 Muscle and ligament activations

In the solution posture, the activations of the four collateral ligament actuators were very low (0.012 or less), indicating that the vast majority of limb stabilization, excluding the metatarsophalangeal joint, was conferred by muscle actuators. However, as the knee and ankle were represented as hinge joints in this study, joint stabilization would also have been achieved in part through resistance offered by these single degree-of-freedom joints to off-axis moments and forces. (Indeed, this resistance could well be responsible for the minimal recruitment of ligaments in the first place.) This resistance was nevertheless transmitted to the bones as joint moments and forces (calculated in the musculoskeletal simulations). Therefore, as far as the bones are concerned, all experienced loads are accounted for and incorporated into the finite element simulations. However, the calculated forces in the collateral ligaments may be appreciably less than what they would be *in vivo*.

The activations of all muscle actuators are presented in Fig. 8D. Most muscles were recruited with activations above 0.1 (i.e., clearly active); no muscle was recruited beyond half of its maximal capacity. The iliotrochanterici medius (ITM) et caudalis (ITC), grastrocnemius medialis (GM) and fibularis longus (FL) were the most recruited muscles, each with an activation above

0.4. The iliofibularis (ILFB), ischiofemoralis (ISF) and caudofemorales partes caudalis (CFC) et pelvica (CFP) were the least recruited muscles, all with negligible activations.

II.4.4 Muscle force sensitivity test

The activations of muscle actuators in the sensitivity test were sometimes markedly different from those of the original simulation (Fig. 8D). However, there was also agreement between the two simulations, where several key hindlimb muscles were predicted to be important in both cases (e.g., ITC, FMTI, GM, GL and FL). Despite the differences in muscle maximum force capabilities between the original and sensitivity test simulations (Table 4), as well as the differences in calculated muscle activations, the stress results differed little from those of the original simulation. The qualitative patterns of stress trajectories were highly similar to those of the original simulation in most regions of the femur, tibiotarsus and fibula. The only region where there was a marked difference was in part of the cranial cnemial crest, in terms of $\boldsymbol{\sigma}_1$ (Fig. 6C,D, cf. Fig. 6A,B). In terms of quantitative results, there was again little deviation in the mean direction of $\boldsymbol{\sigma}_3$ from that calculated for the original simulation (Fig. 5I,J, orange dots). The difference in mean $\boldsymbol{\sigma}_3$ directions between the original and sensitivity test simulations was very small in both the femoral head (1.3°) and medial femoral condyle (5.6°). These results suggest that the approach of assigning a single constant value of 2BW for muscle maximum force capacity does not introduce a significant degree of error, at least as far as the objectives of the present study are concerned.

II.5 Discussion

The aim of this study was to verify the 'reverse' application of the trajectorial theory, to go from observed cancellous bone architectural patterns to bone loading regimes and limb postures, as applied to theropod locomotor biomechanics. This was achieved through the development of a novel approach that integrated musculoskeletal and finite element simulations of a modern

theropod, the chicken. By focusing on a modern theropod here, the validity of the reverse approach was able to examined for each major bone in the hindlimb.

II.5.1 Successes and pitfalls

Despite the many modelling simplifications made in the current study, and that only a single static posture was modelled for any one test, much of the observed cancellous bone architectural patterns in the avian hindlimb was able to be replicated in the principal stress trajectories. This was particularly true of the femur. The 'solution posture' that produced the greatest correspondence between principal stresses and cancellous bone architecture is qualitatively comparable to the posture of the avian hindlimb at around the mid-stance of locomotion (Abourachid & Renous 2000; Gatesy 1999a; Grossi et al. 2014; Reilly 2000; Rubenson et al. 2007; Stoessel & Fischer 2012), especially for medium-sized birds such as chickens and guineafowl. Furthermore, its degree of crouch was almost identical to what would be empirically predicted based on limb bone lengths, for a quiet standing posture (Bishop et al. in review-a). Other aspects of the solution posture also showed correspondence with empirical data for avian terrestrial locomotion. The femur was predicted to be loaded in considerable torsion, with a positive sense, as well as bending of a predominantly anteroposterior nature. This is consistent with the loading regimes recorded by *in vivo* strain gauge studies of chickens and emus (Carrano 1998; Carrano & Biewener 1999; Main & Biewener 2007). Additionally, the two most strongly recruited muscles in the musculoskeletal simulations, the gastrocnemius medialis and fibularis longus, are also the two largest muscles in the distal hindlimb of birds (Lamas et al. 2014; Paxton et al. 2010; Smith et al. 2006), and would therefore be expected to be capable of producing large amounts of force, all other factors being equal.

There were also a few aspects in which the solution posture did not accord well with empirical observations. Most pertinently, the principal stress trajectories in the distal tibiotarsus did not show much correspondence with the cancellous bone architecture observed in this region of the bone of birds (Part I). This may suggest that the manner in which that part of the bone was modelled in the current study was inadequate, that is, too non-physiological. For instance, the

954 ankle joint moment calculated in the musculoskeletal simulations was unable to be applied in the
955 finite element simulations in their current formulation. The discrepancy may also be due to the
956 cancellous bone architecture of the distal tibiotarsus reflecting many different loading regimes,
957 any single one of which cannot capture the architecture. Some of those loading regimes may be
958 very different to that occurring around the mid-stance of locomotion, such as those associated
959 with the swing phase of locomotion, or even standing and sitting. Alternatively, the poor
960 correspondence may indicate that the trajectorial theory may not actually hold true here for some
961 reason, potentially related to the ontogenetic fusion of the proximal tarsals and distal tibia of
962 birds (see Lovejoy 2004; Lovejoy et al. 2002). A second aspect in which the solution posture did
963 not concur with empirical observations concerned the stresses at the tibial mid-shaft. Here, the
964 bone was predicted to be loaded in only minimal torsion, the sense of which was positive; this
965 does not accord with *in vivo* strain gauge studies, which have shown that the avian tibiotarsus
966 experiences a large amount of torsional loading during locomotion, which furthermore is of a
967 negative sense (Biewener et al. 1986; Main & Biewener 2007; Verner et al. 2016). It is possible
968 that if additional degrees of freedom were assigned to the model (e.g., long-axis rotation in the
969 knee; Kambic et al. 2014), more accurate results may have been achieved here.
970
971 A final incongruence between the solution posture and empirical observations was the negligible
972 recruitment of some muscles in the static optimization routine of the musculoskeletal simulations.
973 There were four such muscles (iliofibularis, ischiofemoralis and caudofemorales partes caudalis
974 et pelvica), yet electromyography data indicates that at least three of these (iliofibularis,
975 ischiofemoralis and caudofemoralis pars caudalis) are active during a significant part of the
976 stance phase (Gatesy 1990; Gatesy 1999b; Jacobson & Hollyday 1982; Marsh et al. 2004). The
977 negligible recruitment of the ischiofemoralis and caudofemorales is consonant with the generally
978 small size of these muscles in birds, but this does not hold for the iliofibularis, which is a quite
979 large (Hudson et al. 1959; Lamas et al. 2014; McGowan 1979; Patak & Baldwin 1998; Paxton et
980 al. 2010; Smith et al. 2006). It is probable that all four muscles were minimally recruited in the
981 static optimization routine on account of (i) all muscle actuators were assigned the same
982 maximum capable force output, and (ii) these four particular muscles have smaller moment arms
983 of hip extension compared to other muscles, such as the flexores crures medialis, lateralis pars
984 pelvica et lateralis pars accessoria (Fig. 8E). That is, the static optimization preferentially

recruited muscles with larger moment arms, such that lower forces, and therefore activations, were required to provide the necessary stabilizing joint moments.

The last two aspects of discrepancy between the solution posture and empirical data may also in part reflect the fact that the musculoskeletal simulations were analysed as quasi-static systems. Dynamic aspects of locomotion, such as inertial forces or relative movement between bones, may lead to increased levels of torsion in the tibiotarsus. The same dynamic effects can also influence the net joint moments required to be stabilized by muscle forces; for instance, active retraction of the hip and flexion of the knee may lead to greater activation of the iliofibularis. Therefore, the activations calculated in the current study are probably most informative for muscles that predominantly confer postural stability, rather than active limb movement (i.e., those that act as brakes or motors; Rankin et al. 2016).

II.5.2 Reconstructing loading regimes and postures in extinct species

Notwithstanding the aforementioned discrepancies, the concept of applying the trajectorial theory in reverse is, overall, well-supported by the results of the present study. The reverse approach therefore has the potential to provide insight into the loading regimes experienced by extinct, non-avian theropods during locomotion, and more broadly the postures used during locomotion.

A number of previous studies have sought to use the architecture of cancellous bone to derive loading conditions experienced *in vivo*, although this has largely been confined to theoretical studies of modern animals. Some of these studies have focused on utilizing the spatial distribution of the bulk density of cancellous bone, to which remodelling algorithms (Bona et al. 2006; Fischer et al. 1995) or artificial neural networks (Campoli et al. 2012; Zadpoor et al. 2013) are applied to retrieve one or more loading regimes. Presently, these studies have only been implemented in two dimensions, and so their efficacy in analysing complex, 3-D geometries or loading regimes (such as torsion) remains to be determined. More importantly for the study of extinct species, however, the process of fossilization will greatly hamper any attempt founded upon the bulk density of cancellous bone. Geological chemical alteration (diagenesis) has the

potential to greatly alter the physical density of a fossil bone, and moreover this alteration may not be uniform across a bone, such that it may be impossible to reconstruct the original patterns of bulk density in the living bone.

Diagenesis does not, however, normally alter the actual *structure* of bone; indeed, fine, cellular-level structures are frequently preserved in the fossil bones of dinosaurs and other vertebrates (Chinsamy-Turan 2005; Houssaye 2014). It is the structural characteristics of cancellous bone architecture that are utilized in the present study, namely, fabric directions. Regardless of alterations to bulk density, so long as the actual structure of cancellous bone is preserved in a given fossil, and can be imaged appropriately, then the approach of the present study is feasible. The structural characteristics of cancellous bone have also been used previously in the deduction of *in vivo* loads, in a series of studies by Christen et al. (2012, 2013a,b, 2015). These studies developed voxel-based micro-finite element models that modelled each individual trabecula of a bone, and sought to determine the loading regime, or combination of loading regimes, that achieved the most uniform distribution of strain energy density across the model. The great geometric complexity of the models used in these studies necessitated immense computational capability; only small bones or parts of larger ones were able to be modelled. The computational requirements would quickly become prohibitively large for the modelling of whole bones of even a modest size. Moreover, such geometric complexity would be impossible to produce for medium-sized or large bones, for which high-resolution CT imagery is currently unattainable. An additional problem faced by these computational studies is that currently only very basic loads are able to be examined, and these are only applied at the joints; muscle forces were not considered.

In light of the above discussion, the advantages of the reverse trajectorial approach developed in the current study are clear. Firstly, it is based on the actual structure of cancellous bone, which is usually resistant to alteration by diagenetic processes. Moreover, the structural information required can be ascertained for specimens of a wide range of sizes; each individual trabecula need not be imaged in excruciating detail. The reverse approach is also easily implemented as a fully 3-D analysis that is relatively computationally inexpensive to perform; using a computer with 32 Gb of memory and a 2.4 GHz processor, no single simulation of the present study took more than

10 minutes to solve. However, the main advantage of the reverse approach is that it explicitly links whole-bone cancellous architecture to whole-limb musculoskeletal mechanics. Thus, cancellous bone architectural patterns can be used to directly test hypotheses of limb posture, muscle control and bone loading mechanics, as will be done in Part III.

II.6 Conclusion

In this study a new, mechanistic approach to reconstructing locomotor biomechanics in theropods was developed and tested. Its underlying concept of applying the trajectorial theory in reverse was overall well-supported by the results of the present study: cancellous bone architecture can be used to derive bone loading regimes, and in turn limb postures. This is achieved through the integration of 3-D musculoskeletal and finite element models with observations of cancellous bone fabric direction.

With just a single, quasi-static posture of a chicken hindlimb, modelled with a number of relatively simple assumptions, a large portion of the observed patterns in cancellous bone architecture in birds was able to be replicated by principal stress trajectories. This posture correlated to those actually used during locomotion in birds, in particular the postures used at around mid-stance of normal terrestrial locomotion. Additionally, other biomechanical aspects of the posture, including loading mechanics of the femur and the activations of certain muscles, corresponded well to empirical data recorded for birds.

The reverse approach therefore holds great promise for better understanding whole-bone and whole-limb musculoskeletal biomechanics in the hindlimbs of non-avian theropods during terrestrial locomotion. The generality of this approach also means that it could also be used to improve understanding of locomotor biomechanics in other extinct tetrapod vertebrate groups as well. As correspondence between principal stresses and cancellous bone architecture was greatest in the femur in the present study, this suggests that the reverse approach will yield the most insight for more proximal limb segments.

II.7 Acknowledgements

The staff of the Geosciences Program of the Queensland Museum is thanked for the provision of workspace and access to literature: A. Rozefelds, K. Spring, R. Lawrence, P. Tierney, J. Wilkinson and D. Lewis. Much appreciation is extended to N. Newman (Queensland X-ray, Brisbane) and R. Lawrence (Queensland Museum, Brisbane) for assistance with CT scanning. All scripts and data used are held in the Geosciences Collection of the Queensland Museum, and will be made available upon request to the Collections Manager.

II.8 References

Abourachid A, Hackert R, Herbin M, Libourel PA, Lambert F, Gioanni H, Provini P, Blazevic P, and Hugel V. 2011. Bird terrestrial locomotion as revealed by 3-D kinematics. *Zoology* 114:360–368.

Abourachid A, and Renous S. 2000. Bipedal locomotion in ratites (Paleognatiform): examples of cursorial birds. *Ibis* 142:538–549.

Adachi T, Tsubota K, Tomita Y, and Hollister SJ. 2001. Trabecular Surface Remodeling Simulation for Cancellous Bone Using Microstructural Voxel Finite Element Models. *Journal of Biomechanical Engineering* 123:403-409.

Alexander RM. 1977. Terrestrial locomotion. In: Alexander RM, and Goldspink G, eds. *Mechanics and Energetics of Animal Locomotion*. London: Chapman and Hall, 168–203.

Allen V, Bates KT, Li Z, and Hutchinson JR. 2013. Linking the evolution of body shape and locomotor biomechanics in bird-line archosaurs. *Nature* 497:104–107.

Allen V, Kambic RE, Gatesy SM, and Hutchinson JR. 2017. Gearing effects of the patella (knee extensor muscle sesamoid) of the helmeted guineafowl during terrestrial locomotion. *Journal of Zoology* 303:178-187.

Allmendinger RW, Cardozo NC, and Fisher D. 2013. *Structural Geology Algorithms: Vectors and Tensors*. Cambridge: Cambridge University Press.

Amson E, Arnold P, van Heteren AH, Canoville A, and Nyakatura JA. 2017. Trabecular architecture in the forelimb epiphyses of extant xenarthrans (Mammalia). *Frontiers in Zoology* 14:52.

Anderson FC, and Pandy MG. 1999. A Dynamic Optimization Solution for Vertical Jumping in Three Dimensions. *Computer Methods in Biomechanics and Biomedical Engineering* 2:201-231.

1116 Anderson FC, and Pandy MG. 2001. Static and dynamic optimization solutions for gait are
1117 practically equivalent. *Journal of Biomechanics* 34:153-161.
1118 Andrada E, Nyakatura JA, Bergmann F, and Blickhan R. 2013. Adjustments of global and local
1119 hindlimb properties during terrestrial locomotion of the common quail (*Coturnix*
1120 *coturnix*). *Journal of Experimental Biology* 216:3906-3916.
1121 Attene M, and Falcidieno B. 2006. ReMESH: An Interactive Environment to Edit and Repair
1122 Triangle Meshes. Proceedings of the Eighth International Conference on Shape Modeling
1123 and Applications. Matushima. p 271-276.
1124 Barak MM, Lieberman DE, and Hublin J-J. 2011. A Wolff in sheep's clothing: Trabecular bone
1125 adaptation in response to changes in joint loading orientation. *Bone* 49:1141-1151.
1126 Barak MM, Lieberman DE, Raichlen DA, Pontzer H, Warrener AG, and Hublin J-J. 2013.
1127 Trabecular Evidence for a Human-Like Gait in *Australopithecus africanus*. *PLoS ONE*
1128 8:e77687.
1129 Beaupré GS, Orr TE, and Carter DR. 1990. An Approach for Time-Dependent Bone Modeling
1130 and Remodeling – Application: A Preliminary Remodeling Simulation. *Journal of*
1131 *Orthopaedic Research* 8:662-670.
1132 Beer FP, Johnston ER, Jr, DeWolf JT, and Mazurek DF. 2012. *Mechanics of Materials*. New
1133 York: McGraw-Hill.
1134 Bergmann G, Deuretzbacher G, Heller M, Graichen F, Rohlmann A, Strauss J, and Duda GN.
1135 2001. Hip contact forces and gait patterns from routine activities. *Journal of*
1136 *Biomechanics* 34:859-871.
1137 Bergmann G, Graichen F, and Rohlmann A. 1999. Hip joint forces in sheep. *Journal of*
1138 *Biomechanics* 32:769-777.
1139 Biewener AA, Fazzalari NL, Konieczynski DD, and Baudinette RV. 1996. Adaptive Changes in
1140 Trabecular Architecture in Relation to Functional Strain Patterns and Disuse. *Bone* 19:1-
1141 8.
1142 Biewener AA, Swartz SM, and Bertram JEA. 1986. Bone Modelling During Growth: Dynamics
1143 Strain Equilibrium in the Chick Tibiotarsus. *Calcified Tissue International* 39:390-395.
1144 Bishop PJ, Clemente CJ, Graham DF, Lamas LP, Hutchinson JR, Rubenson J, Hancock JA,
1145 Wilson RS, Hocknull SA, Barrett RS, and Lloyd DG. in review-a. The Influence of
1146 Speed and Size on Avian Terrestrial Locomotor Biomechanics: Predicting Locomotion in
1147 Extinct Theropod Dinosaurs. *PLoS ONE*.
1148 Bishop PJ, Clemente CJ, Weems RE, Graham DF, Lamas LP, Hutchinson JR, Rubenson J,
1149 Wilson RS, Hocknull SA, Barrett RS, and Lloyd DG. 2017. Using step width to compare
1150 locomotor biomechanics between extinct, non-avian theropod dinosaurs and modern
1151 obligate bipeds. *Journal of the Royal Society Interface* 14:20170276.
1152 Bishop PJ, Hocknull SA, Clemente CJ, Hutchinson JR, Farke AA, Barrett RS, and Lloyd DG. in
1153 review-b. Cancellous bone architecture and theropod dinosaur locomotion. Part III –
1154 Inferring posture and locomotor biomechanics in extinct theropods, and its evolution on
1155 the line to birds. *PeerJ*.
1156 Bishop PJ, Hocknull SA, Clemente CJ, Hutchinson JR, Farke AA, Beck BR, Barrett RS, and
1157 Lloyd DG. in review-c. Cancellous bone architecture and theropod dinosaur locomotion.
1158 Part I – An examination of cancellous bone architecture in the hindlimb bones of
1159 theropods. *PeerJ*.

Blob RW, and Biewener AA. 2001. Mechanics of limb bone loading during terrestrial locomotion in the green iguana (*Iguana iguana*) and American alligator (*Alligator mississippiensis*). *Journal of Experimental Biology* 204:1099-1122.

Bona MA, Martin LD, and Fischer KJ. 2006. A contact algorithm for density-based load estimation. *Journal of Biomechanics* 39:636-644.

Bonnan MF, Sandrik JL, Nishiwaki T, Wilhite DR, Elsey RM, and Vittore C. 2010. Calcified Cartilage Shape in Archosaur Long Bones Reflects Overlying Joint Shape in Stress-Bearing Elements: Implications for Nonavian Dinosaur Locomotion. *The Anatomical Record* 293:2044-2055.

Bonnan MF, Wilhite DR, Masters SL, Yates AM, Gardner CK, and Aguiar A. 2013. What Lies Beneath: Sub-Articular Long Bone Shape Scaling in Eutherian Mammals and Saurischian Dinosaurs Suggests Different Locomotor Adaptations for Gigantism. *PLoS ONE* 8:e75216.

Boyle C, and Kim IY. 2011. Three-dimensional micro-level computational study of Wolff's law via trabecular bone remodeling in the human proximal femur using design space topology optimization. *Journal of Biomechanics* 44:935-942.

Brassey CA, Maidment SCR, and Barrett PM. 2017. Muscle moment arm analyses applied to vertebrate paleontology: a case study using *Stegosaurus stenops* Marsh, 1887. *Journal of Vertebrate Paleontology* 37:e1361432.

Bright JA. 2014. A review of paleontological finite element models and their validity. *Journal of Paleontology* 88:760-769.

Bright JA, and Rayfield EJ. 2011. The Response of Cranial Biomechanical Finite Element Models to Variations in Mesh Density. *The Anatomical Record* 294:610-620.

Bryant JD, Bennett MB, Brust J, and Alexander RM. 1987. Forces exerted on the ground by galloping dogs (Canis familiaris). *Journal of Zoology* 213:193-203.

Butcher MT, and Blob RW. 2008. Mechanics of limb bone loading during terrestrial locomotion in river cooter turtles (*Pseudemys concinna*). *Journal of Experimental Biology* 211:1187-1202.

Calow LJ, and Alexander RM. 1973. A mechanical analysis of a hind leg of a frog (*Rana temporaria*). *Journal of Zoology* 171:293-321.

Campoli G, Weinans H, and Zadpoor AA. 2012. Computational load estimation of the femur. *Journal of the Mechanical Behaviour of Biomedical Materials* 10:108-119.

Cardozo NC, and Allmendinger RW. 2013. Spherical projections with OSXStereonet. *Computers & Geosciences* 51:193-205.

Carey RE, Zheng L, Aiyangar AK, Harner CD, and Zhang X. 2014. Subject-Specific Finite Element Modeling of the Tibiofemoral Joint Based on CT, Magnetic Resonance Imaging and Dynamic Stereo-Radiography Data in Vivo. *Journal of Biomechanical Engineering* 136:041004-041001.

Carrano MT. 1998. Locomotion in non-avian dinosaurs: integrating data from hindlimb kinematics, in vivo strains, and bone morphology. *Paleobiology* 24:450-469.

Carrano MT, and Biewener AA. 1999. Experimental Alteration of Limb Posture in the Chicken (*Gallus gallus*) and its Bearing on the Use of Birds as Analogs for Dinosaur Locomotion. *Journal of Morphology* 240:237-249.

Carrano MT, and Hutchinson JR. 2002. Pelvic and hindlimb musculature of *Tyrannosaurus rex* (Dinosauria: Theropoda). *Journal of Morphology* 253:207-228.

Carter DR, and Beaupré GS. 2001. *Skeletal Function and Form: Mechanobiology of Skeletal Development, Aging, and Regeneration*. Cambridge: Cambridge University Press.

Carter DR, Orr TE, and Fyhrie DP. 1989. Relationships between loading history and femoral cancellous bone architecture. *Journal of Biomechanics* 22:231-244.

Chadwick KP, Regnault S, Allen V, and Hutchinson JR. 2014. Three-dimensional anatomy of the ostrich (*Struthio camelus*) knee joint. *PeerJ* 2:e706.

Charles JP, Cappellari O, Spence AJ, Hutchinson JR, and Wells DJ. 2016. Musculoskeletal Geometry, Muscle Architecture and Functional Specialisations of the Mouse Hindlimb. *PLoS ONE* 11:e147669.

Chinsamy-Turan A. 2005. *The Microstructure of Dinosaur Bone*. Baltimore: Johns Hopkins University Press.

Christen P, Ito K, dos Santos AA, Müller R, and van Rietbergen B. 2013a. Validation of a bone loading estimation algorithm for patient-specific bone remodelling simulations. *Journal of Biomechanics* 46:941-948.

Christen P, Ito K, Galis F, and van Rietbergen B. 2015. Determination of hip-joint loading patterns of living and extinct mammals using an inverse Wolff's law approach. *Biomechanics and Modeling in Mechanobiology* 14:427-432.

Christen P, Ito K, Knippels I, Müller R, van Lenthe GH, and van Rietbergen B. 2013b. Subject-specific bone loading estimation in the human distal radius. *Journal of Biomechanics* 46:759-766.

Christen P, van Rietbergen B, Lambers FM, Müller R, and Ito K. 2012. Bone morphology allows estimation of loading history in a murine model of bone adaptation. *Biomechanics and Modeling in Mechanobiology* 11:483-492.

Coelho PG, Fernandes PR, Rodrigues HC, Cardoso JB, and Guedes JM. 2009. Numerical modeling of bone tissue adaptation—A hierarchical approach for bone apparent density and trabecular structure. *Journal of Biomechanics* 42:830-837.

Cowin SC. 2001. The false premise in Wolff's Law. In: Cowin SC, ed. *Bone Biomechanics Handbook*. 2 ed. Boca Raton: CRC Press, 30-31–30-15.

Currey JD. 2002. *Bones: Structure and Mechanics*. Princeton: Princeton University Press.

Delp SL, Anderson FC, Arnold AS, Loan P, Habib A, John CT, Guendelman E, and Thelen DG. 2007. OpenSim: Open-Source Software to Create and Analyze Dynamic Simulations of Movement. *IEEE Transactions of Biomedical Engineering* 54:1940-1950.

Delp SL, Loan P, Hoy MG, Zajac FE, Topp EL, and Rosen JM. 1990. An Interactive Graphics-Based Model of the Lower Extremity to Study Orthopaedic Surgical Procedures. *IEEE Transactions of Biomedical Engineering* 37:757-767.

Dumont ER, Piccirillo J, and Grosse IR. 2005. Finite-Element Analysis of Biting Behaviour and Bone Stress in the Facial Skeletons of Bats. *The Anatomical Record* 283A:319-330.

Erickson GM, Catanese J, III, and Keaveny TM. 2002. Evolution of the Biomechanical Properties of the Femur. *The Anatomical Record* 268:115-124.

Fajardo RJ, and Müller R. 2001. Three-Dimensional Analysis of Nonhuman Primate Trabecular Architecture Using Micro-Computed Tomography. *American Journal of Physical Anthropology* 115:327-336.

Fernandez JW, Mithraratne P, Thrupp SF, Tawhai MH, and Hunter PJ. 2004. Anatomically based geometric modelling of the musculo-skeletal system and other organs. *Biomechanics and Modeling in Mechanobiology* 2:139-155.

1250 Fischer KJ, Jacobs CR, and Carter DR. 1995. Computational method for determination of bone
1251 and joint loads using bone density distributions. *Journal of Biomechanics* 28:1127-1135.
1252 Gatesy SM. 1990. Caudofemoral musculature and the evolution of theropod locomotion.
1253 *Paleobiology* 16:170-186.
1254 Gatesy SM. 1994. Neuromuscular Diversity in Archosaur Deep Dorsal Thigh Muscles. *Brain,*
1255 *Behavior and Evolution* 43:1-14.
1256 Gatesy SM. 1999a. Guineafowl Hindlimb Function I: Cineradiographic Analysis and Speed
1257 Effects. *Journal of Morphology* 240:115–125.
1258 Gatesy SM. 1999b. Guineafowl Hindlimb Function II: Electromyographic Analysis and Motor
1259 Pattern Evolution. *Journal of Morphology* 240:127–142.
1260 Gefen A, and Seliktar R. 2004. Comparison of the trabecular architecture and the isostatic stress
1261 flow in the human calcaneus. *Medical Engineering & Physics* 26:119-129.
1262 Geraldes DM, Modenese L, and Phillips ATM. 2016. Consideration of multiple load cases is
1263 critical in modelling orthotropic bone adaptation in the femur. *Biomechanics and*
1264 *Modeling in Mechanobiology* 15:1029-1042.
1265 Geraldes DM, and Phillips ATM. 2014. A comparative study of orthotropic and isotropic bone
1266 adaptation in the femur. *International Journal for Numerical Methods in Biomedical*
1267 *Engineering* 30:873-889.
1268 Giarmatzis G, Jonkers I, Wesseling M, Van Rossom S, and Verschueren S. 2015. Loading of Hip
1269 Measured by Hip Contact Forces at Different Speeds of Walking and Running. *Journal of*
1270 *Bone and Mineral Research* 30:1431-1440.
1271 Giddings VL, Beaupré GS, Whalen RT, and Carter DR. 2000. Calcaneal loading during walking
1272 and running. *Medicine & Science in Sports & Exercise* 32:627-634.
1273 Gilbert MM, Snively E, and Cotton J. 2016. The Tarsometatarsus of the Ostrich *Struthio*
1274 *camelus*: Anatomy, Bone Densities, and Structural Mechanics. *PLoS ONE* 11:e0149708.
1275 Goetz JA, Derrick TR, Pedersen DR, Robinson DA, Conzemius MG, Baer TE, and Brown TD.
1276 2008. Hip joint contact force in the emu (*Dromaius novaehollandiae*) during normal level
1277 walking. *Journal of Biomechanics* 41:770-778.
1278 Goldstein SA, Matthews LS, Kuhn JL, and Hollister SJ. 1991. Trabecular bone remodelling: an
1279 experimental model. *Journal of Biomechanics* 24 (suppl. 1):135-150.
1280 Gosnell WC, Butcher MT, Maie T, and Blob RW. 2011. Femoral loading mechanics in the
1281 Virginia opossum, *Didelphis virginiana*: torsion and mediolateral bending in mammalian
1282 locomotion. *Journal of Experimental Biology* 214:3455-3466.
1283 Griffin NL, D'Août K, Ryan TM, Richmond BG, Ketcham RA, and Postnov A. 2010.
1284 Comparative forefoot trabecular bone architecture in extant hominids. *Journal of Human*
1285 *Evolution* 59:202-213.
1286 Grossi B, Iriarte-Díaz J, Larach O, Canals M, and Vásquez RA. 2014. Walking Like Dinosaurs:
1287 Chickens with Artificial Tails Provide Clues about Non-Avian Theropod Locomotion.
1288 *PLoS ONE* 9:e88458.
1289 Guldman RE, Richards M, Caldwell NJ, Kuelske CL, and Goldstein SA. 1997. Trabecular bone
1290 adaptation to variations in porous-coated implant topology. *Journal of Biomechanics*
1291 30:147-153.
1292 Haines RW. 1942. The tetrapod knee joint. *Journal of Anatomy* 76:270-301.
1293 Hayes WC, and Snyder B. 1981. Toward a quantitative formulation of Wolff's Law in trabecular
1294 bone. In: Cowin SC, ed. *Mechanical Properties of Bone*. New York: American Society of
1295 Mechanical Engineers, 43-68.

1296 Hébert D, Lebrun R, and Marivaux L. 2012. Comparative Three-Dimensional Structure of the
1297 Trabecular Bone in the Talus of Primates and Its Relationship to Ankle Joint Loads
1298 Generated During Locomotion. *The Anatomical Record* 295:2069-2088.
1299 Houssaye A. 2014. Advances in vertebrate palaeohistology: recent progress, discoveries, and
1300 new approaches. *Biological Journal of the Linnean Society* 112:645-648.
1301 Hudson GE. 1937. Studies on the Muscles of the Pelvic Appendage in Birds. *American Midland*
1302 *Naturalist* 18:1-108.
1303 Hudson GE, Lanzillotti PJ, and Edwards GD. 1959. Muscles of the Pelvic Limb in Galliform
1304 Birds. *American Midland Naturalist* 61:1-67.
1305 Huiskes R, Ruimerman R, van Lenthe GH, and Janssen JD. 2000. Effects of mechanical forces
1306 on maintenance and adaptation of form in trabecular bone. *Nature* 405:704-706.
1307 Hutchinson JR. 2002. The evolution of hindlimb tendons and muscles on the line to crown-group
1308 birds. *Comparative Biochemistry and Physiology, Part A* 133:1051-1086.
1309 Hutchinson JR. 2004. Biomechanical Modeling and Sensitivity Analysis of Bipedal Running
1310 Ability. I. Extant Taxa. *Journal of Morphology* 262:421-440.
1311 Hutchinson JR, and Allen V. 2009. The evolutionary continuum of limb function from early
1312 theropods to birds. *Naturwissenschaften* 96:423-448.
1313 Hutchinson JR, Anderson FC, Blemker SS, and Delp SL. 2005. Analysis of hindlimb muscle
1314 moment arms in *Tyrannosaurus rex* using a three-dimensional musculoskeletal computer
1315 model: implications for stance, gait, and speed. *Paleobiology* 31:676-701.
1316 Hutchinson JR, Miller CE, Fritsch G, and Hildebrandt T. 2008. The Anatomical Foundation for
1317 Multidisciplinary Studies of Animal Limb Function: Examples from Dinosaur and
1318 Elephant Limb Imaging Studies. In: Endo H, and Frey R, eds. *Anatomical Imaging:*
1319 *Towards a New Morphology*. Tokyo: Springer, 23-38.
1320 Hutchinson JR, Rankin JW, Rubenson J, Rosenbluth KH, Siston RA, and Delp SL. 2015.
1321 Musculoskeletal Modelling of an ostrich (*Stuthio camelus*) pelvic limb: influence of limb
1322 orientation of muscular capacity during locomotion. *PeerJ* 3:e1001.
1323 Jacobs CR. 2000. The mechanobioogy of cancellous bone structural adaptation. *Journal of*
1324 *Rehabilitation Research and Development* 37:209-216.
1325 Jacobs CR, Simo JC, Beaupré GS, and Carter DR. 1997. Adaptive bone remodeling
1326 incorporating simultaneous density and anisotropy considerations. *Journal of*
1327 *Biomechanics* 30:603-613.
1328 Jacobson RD, and Hollyday M. 1982. A Behavioural and Electromyographic Study of Walking
1329 in the Chick. *Journal of Neurophysiology* 48:238-256.
1330 Jang IG, and Kim IY. 2008. Computational study of Wolff's law with trabecular architecture in
1331 the human proximal femur using topology optimization. *Journal of Biomechanics*
1332 41:2353-2361.
1333 Jang IG, and Kim IY. 2010a. Application of design space optimization to bone remodeling
1334 simulation of trabecular architecture in human proximal femur for higher computational
1335 efficiency. *Finite Elements in Analysis and Design* 46:311-319.
1336 Jang IG, and Kim IY. 2010b. Computational simulation of cortical and trabecular bone change in
1337 human proximal femur during bone remodelling. *Journal of Biomechanics* 43:294-301.
1338 Kabel J, van Rietbergen B, Odgaard A, and Huiskes R. 1999. Constitutive Relationships of
1339 Fabric, Density, and Elastic Properties in Cancellous Bone Architecture. *Bone* 25:481-
1340 486.

1341 Kambic RE, Roberts TJ, and Gatesy SM. 2014. Long-axis rotation: a missing degree of freedom
1342 in avian bipedal locomotion. *Journal of Experimental Biology* 217:2770-2782.
1343 Kazemi M, Dabiri Y, and Li LP. 2013. Recent Advances in Computational Mechanics of the
1344 Human Knee Joint. *Computational and Mathematical Methods in Medicine*
1345 2013:718423.
1346 Kivell TL. 2016. A review of trabecular bone functional adaptation: what have we learned from
1347 trabecular analyses in extant hominoids and what can we apply to fossils? *Journal of*
1348 *Anatomy* 228:569-594.
1349 Koch JC. 1917. The laws of bone architecture. *American Journal of Anatomy* 21:177-298.
1350 Lamas LP, Main RP, and Hutchinson JR. 2014. Ontogenetic scaling patterns and functional
1351 anatomy of the pelvic limb musculature in emus (*Dromaius novaehollandiae*). *PeerJ*
1352 2:e716.
1353 Lanyon LE. 1974. Experimental support for the trajectorial theory of bone structure. *Journal of*
1354 *Bone and Joint Surgery* 56B:160-166.
1355 Lanyon LE. 1996. Locomotor Loading and Functional Adaptation in Limb Bones. *Symposium of*
1356 *the Zoological Society of London* 48:305-329.
1357 Lerner ZF, Gadomski BC, Ipson AK, Haussler KK, Puttlitz CM, and Browning RC. 2015.
1358 Modulating Tibiofemoral Contact Force in the Sheep Hind Limb via Treadmill Walking:
1359 Predictions From an Opensim Musculoskeletal Model. *Journal of Orthopaedic Research*
1360 33:1128-1133.
1361 Liao L. 2011. A Study of Inertia Relief Analysis. 52nd AIAA/ASME/ASCE/AHS/ASC
1362 Structures, Structural Dynamics and Materials Conference. Denver. p AIAA 2011-2002.
1363 Lovejoy CO. 2004. The natural history of human gait and posture. Part 2. Hip and thigh. *Gait &*
1364 *Posture* 21:113-124.
1365 Lovejoy CO, Meindl RS, Ohman JC, Heiple KG, and White TD. 2002. The Maka Femur and Its
1366 Bearing on the Antiquity of Human Walking: Applying Contemporary Concepts of
1367 Morphogenesis to the Human Fossil Record. *American Journal of Physical Anthropology*
1368 119:97-133.
1369 MacLatchy L, and Müller R. 2002. A comparison of the femoral head and neck trabecular
1370 architecture of *Galago* and *Perodicticus* using micro-computed tomography (μCT).
1371 *Journal of Human Evolution* 43:89-105.
1372 Maga M, Kappelman J, Ryan TM, and Ketcham RA. 2006. Preliminary Observations on the
1373 Calcaneal Trabecular Microarchitecture of Extant Large-Bodied Hominoids. *American*
1374 *Journal of Physical Anthropology* 129:410-417.
1375 Main RP, and Biewener AA. 2007. Skeletal strain patterns and growth in the emu hindlimb
1376 during ontogeny. *Journal of Experimental Biology* 210:2676-2690.
1377 Marsh RL, Ellerby DJ, Carr JA, Henry HT, and Buchanan CI. 2004. Partitioning the Energetics
1378 of Walking and Running: Swinging the Limbs is Expensive. *Science* 303:80-83.
1379 Martelli S, Taddei F, Testi D, Delp SL, and Viceconti M. 2011. NMSBuilder: an application to
1380 personalize NMS models. Proceedings of the 23rd Congress of the International Society
1381 of Biomechanics. Brussels.
1382 Matarazzo SA. 2015. Trabecular Architecture of the Manual Elements Reflects Locomotor
1383 Patterns in Primates. *PLoS ONE* 10:e0120436.
1384 McGowan C. 1979. The Hind Limb Musculature of the brown Kiwi, *Apteryx australis mantelli*.
1385 *Journal of Morphology* 160:33-74.

McHenry CR, Wroe S, Clausen PD, Moreno K, and Cunningham E. 2007. Supermodeled sabercat, predatory behaviour in *Smilodon fatalis* revealed by high-resolution 3D computer simulation. *Proceedings of the National Academy of Sciences* 104:16010-16015.

Medler S. 2002. Comparative trends in shortening velocity and force production in skeletal muscle. *American Journal of Physiology* 283:R368-R378.

Miller Z, Fuchs MB, and Arcan M. 2002. Trabecular bone adaptation with an orthotropic material model. *Journal of Biomechanics* 35:247-256.

Modenese L, and Phillips ATM. 2012. Prediction of hip contact forces and muscle activations during walking at different speeds. *Multibody System Dynamics* 28:157-168.

Mullender MG, and Huiskes R. 1995. Proposal for the Regulatory Mechanism of Wolff's Law. *Journal of Orthopaedic Research* 13:503-512.

O'Neill MC, Lee L-F, Larson SG, Demes B, Stern JT, Jr, and Umberger BR. 2013. A three-dimensional musculoskeletal model of the chimpanzee (*Pan troglodytes*) pelvis and hindlimb. *Journal of Experimental Biology* 216:3709-3723.

Odgaard A, Kabel J, van Rietbergen B, Dalstra M, and Huiskes R. 1997. Fabric and elastic principal directions of cancellous bone are closely related. *Journal of Biomechanics* 30:487-495.

Page AE, Allan C, Jasty M, Harrigan TP, Bragdon CR, and Harris WH. 1993. Determination of loading parameters in the canine hip *in vivo*. *Journal of Biomechanics* 26.

Patak AE, and Baldwin J. 1998. Pelvis Limb Musculature in the Emu *Dromaius novaehollandiae* (Aves: Struthioniformes: Dromaiidae): Adaptations to High-Speed Running. *Journal of Morphology* 238:23-37.

Pauwels F. 1980. *Biomechanics of the Locomotor Apparatus*. Berlin: Springer-Verlag.

Paxton H, Anthony NB, Corr SA, and Hutchinson JR. 2010. The effects of selective breeding on the architectural properties of the pelvic limb in broiler chickens: a comparative study across modern and ancestral populations. *Journal of Anatomy* 217:153-166.

Pedotti A, Krishnan VV, and Stark L. 1978. Optimization of Muscle-Force Sequencing in Human Locomotion. *Mathematical Biosciences* 38:57-76.

Phillips ATM, Villette CC, and Modenese L. 2015. Femoral bone mesoscale structural architecture prediction using musculoskeletal and finite element modelling. *International Biomechanics* 2:43-61.

Polk JD, Blumenfeld J, and Ahluwalia D. 2008. Knee Posture Predicted From Subchondral Apparent Density in the Distal Femur: An Experimental Validation. *The Anatomical Record* 16:323-329.

Pontzer H, Lieberman DE, Momin E, Devlin MJ, Polk JD, Hallgrímsson B, and Cooper DML. 2006. Trabecular bone in the bird knee responds with high sensitivity to changes in load orientation. *Journal of Experimental Biology* 209:57-65.

Radin EL, Orr RB, Kelman JL, Paul IL, and Rose RM. 1982. Effect of prolonged walking on concrete on the knees of sheep. *Journal of Biomechanics* 15:487-492.

Rankin JW, Rubenson J, and Hutchinson JR. 2016. Inferring muscle functional roles of the ostrich pelvic limb during walking and running using computer optimizaion. *Journal of the Royal Society Interface* 13:20160035.

Reed KL, and Brown TD. 2001. Elastic modulus and strngth of emu cortical bone. *The Iowa Orthopaedic Journal* 21:53-57.

Regnault S, Allen VR, Chadwick KP, and Hutchinson JR. 2017. Analysis of the moment arks and kinematics of ostrich (*Struthio camelus*) double patellar sesamoids. *Journal of Experimental Zoology* 327:163-171.

Reilly SM. 2000. Locomotion in the Quail (*Coturnix japonica*): The Kinematics of Walking and Increasing Speed. *Journal of Morphology* 243:173-185.

Ren L, Miller CE, Lair R, and Hutchinson JR. 2010. Integration of biomechanical compliance, leverage, and power in elephant limbs. *Proceedings of the National Academy of Sciences* 107:7078-7082.

Richmond BG, Nakatsukasa M, Griffin NL, Ogihara N, and Ketcham RA. 2005. Trabecular bone structure in a bipedally trained macaque. Seventy-Fourth Annual Meeting of the American Association of Physical Anthropologists, April 6–9, 2005. Milwaukee, United States of America. p 175-176.

Roberts TJ, Chen MS, and Taylor CR. 1998. Energetics of bipedal running. II. Limb design and running mechanics. *Journal of Experimental Biology* 205:2753-2762.

Rubenson J, Lloyd DG, Besier TF, Heliams DB, and Fournier PA. 2007. Running in ostriches (*Stuthio camelus*): three-dimensional joint axes alignment and joint kinematics. *Journal of Experimental Biology* 210:2548-2562.

Rubenson J, Lloyd DG, Heliams DB, Besier TF, and Fournier PA. 2011. Adaptations for economical bipedal running: the effect of limb structure on three-dimensional joint mechanics. *Journal of the Royal Society Interface* 8:740-755.

Rudman KE, Aspden RM, and Meakin JR. 2006. Compression or tension? The stress distribution in the proximal femur. *BioMedical Engineering OnLine* 5:12.

Ruimerman R, Hilbers P, van Rietbergen B, and Huiskes R. 2005. A theoretical framework for strain-related trabecular bone maintenance and adaptation. *Journal of Biomechanics* 38:931-941.

Ryan TM, and Ketcham RA. 2002. The three-dimensional structure of trabecular bone in the femoral head of strepsirrhine primates. *Journal of Human Evolution* 43:1-26.

Ryan TM, and Ketcham RA. 2005. Angular Orientation of Trabecular Bone in the Femoral Head and Its Relationship to Hip Joint Loads in Leaping Primates. *Journal of Morphology* 265:249-263.

Ryan TM, and Shaw CN. 2012. Unique Suites of Trabecular Bone Features Characterize Locomotor Behavior in Human and Non-Human Anthropoid Primates. *PLoS ONE* 7:e41037.

Schaller NU, D'Août K, Villa R, Herkner B, and Aerts P. 2011. Toe function and dynamic pressure distribution in ostrich locomotion. *Journal of Experimental Biology* 214:1123-1130.

Sheffield KM, and Blob RW. 2011. Loading mechanics of the femur in tiger salamanders (*Ambystoma tigrinum*) during terrestrial locomotion. *Journal of Experimental Biology* 214:2603-2615.

Smith NC, Wilson AM, Jespers KJ, and Payne RC. 2006. Muscle architecture and functional anatomy of the pelvic limb of the ostrich (*Struthio camelus*). *Journal of Anatomy* 209:765-779.

Steele KM, DeMers MS, Schwartz MH, and Delp SL. 2012. Compressive tibiofemoral force during crouch gait. *Gait & Posture* 35:556-560.

Stoessel A, and Fischer MS. 2012. Comparative intralimb coordination in avian bipedal locomotion. *Journal of Experimental Biology* 215:4055-4069.

Stops A, Wilcox R, and Jin Z. 2012. Computational modelling of the natural hip: a review of finite element and multibody simulations. *Computer Methods in Biomechanics and Biomedical Engineering* 15:963-979.

Su A, Wallace IJ, and Nakatsukasa M. 2013. Trabecular bone anisotropy and orientation in an Early Pleistocene hominin talus from East Turkana, Kenya. *Journal of Human Evolution* 64:667-677.

Su SC, Skedros JG, Bachus KN, and Bloebaum RD. 1999. Loading conditions and cortical bone construction of an artiodactyl calcaneus. *Journal of Experimental Biology* 202:3239-3254.

Sverdlova N. 2011. Tensile trabeculae - Myth or Reality? *Journal of Musculoskeletal and Neuronal Interactions* 11:1-7.

Taylor SJG, and Walker PS. 2001. Forces and moments telemetered from two distal femoral replacements during various activities. *Journal of Biomechanics* 34:839-848.

Tsegai ZJ, Kivell TL, Gross T, Nguyen NH, Pahr DH, Smaers JB, and Skinner MM. 2013. Trabecular Bone Structure Correlates with Hand Posture and Use in Hominoids. *PLoS ONE* 8:e78781.

Tsubota K, Adachi T, and Tomita Y. 2002. Functional adaptation of cancellous bone in human proximal femur predicted by trabecular surface remodeling simulation toward uniform stress state. *Journal of Biomechanics* 35:1541-1551.

Tsubota K, Suzuki Y, Yamada T, Hojo M, Makinouchi A, and Adachi T. 2009. Computer simulation of trabecular remodelling in human proximal femur using large-scale voxel FE models: Approach to understanding Wolff's law. *Journal of Biomechanics* 42:1088-1094.

Turner CH. 1998. Three Rules for Bone Adaptation to Mechanical Stimuli. *Bone* 23:399-407.

Turner CH, Anne V, and Pidaparti RMV. 1997. A uniform strain criterion for trabecular bone adaptation: do continuum-level strain gradients drive adaptation? *Journal of Biomechanics* 30:555-563.

Turner CH, Cowin SC, Rho JY, Ashman RB, and Rice JC. 1990. The fabric dependence of the orthotropic elastic constants of cancellous bone. *Journal of Biomechanics* 23:549-561.

Ulrich D, van Rietbergen B, Laib A, and Rüegsegger P. 1999. The Ability of Three-Dimensional Structural Indices to Reflect Mechanical Aspects of Trabecular Bone. *Bone* 25:55-60.

Valente G, Pitto L, Testi D, Seth A, Delp SL, Stagni R, Viceconti M, and Taddei F. 2014. Are Subject-Specific Musculoskeletal Models Robust to the Uncertainties in Parameter Identification? *PLoS ONE* 9:e112625.

van Arkel RJ, Modenese L, Phillips ATM, and Jeffers JRT. 2013. Hip Abduction Can Prevent Posterior Edge Loading of Hip Replacements. *Journal of Orthopaedic Research* 31:1172-1179.

van der Meulen MCH, Morgan TG, Yang X, Baldini TH, Myers ER, Wright TM, and Bostrom MPG. 2006. Cancellous bone adaptation to in vivo loading in a rabbit model. *Bone* 38:871-877.

van der Meulen MCH, Yang X, Morgan TG, and Bostrom MPG. 2009. The Effects of Loading on Cancellous Bone in the Rabbit. *Clinical Orthopaedics and Related Research* 467:2000-2006.

Vander Sloten J, and Van der Perre G. 1989. Trabecular structure compared to stress trajectories in the proximal femur and calcaneus. *Journal of Biomedical Engineering* 11:203-208.

Verner KA, Lehner M, Lamas LP, and Main RP. 2016. Experimental tests of planar strain theory for predicting cross-sectional longitudinal and shear strains. *Journal of Experimental Biology* 219:3082-3090.

Volpato V, Viola TB, Nakatsusaka M, Bondioli L, and Macchiarelli R. 2008. Textural characteristics of the iliac-femoral trabecular pattern in a bipedally trained Japanese macaque. *Primates* 49:16-25.

Wang H, Ji B, Liu XS, Guo XE, Huang Y, and Hwang K-C. 2012. Analysis of microstructural and mechanical alterations of trabecular bone in a simulated three-dimensional remodelling process. *Journal of Biomechanics* 45:2417-2425.

Wink CS, Elsey RM, St Onge M, and Zimny MI. 1989. Neural Element in the Cruciate Ligaments and Menisci of the Knee Joint of the American Alligator, *Alligator mississippiensis*. *Journal of Morphology* 202:165-172.

Winter DA. 2009. *Biomechanics and Motor Control of Human Movement*. Hoboken: John Wiley & Sons, Inc.

Witte TH, Knill K, and Wilson AM. 2004. Determination of peak vertical ground reaction force from duty factor in the horse (*Equus caballus*). *Journal of Experimental Biology* 207:3639-3648.

Wolff J. 1892. *Das Gesetz der Transformation der Knochen*. Berlin: August Hirschwald.

Wroe S, Moreno K, Clausen PD, McHenry CR, and Curnoe D. 2007. High-Resolution Three-Dimensional Computer Simulation of Hominid Cranial Mechanics. *The Anatomical Record* 290:1248-1255.

Zadpoor AA, Campoli G, and Weinans H. 2013. Neural network prediction of load from the morphology of trabecular bone. *Applied Mathematical Modelling* 37:5260-5276.

Zinoviev AV. 2010. *Comparative anatomy, structural modifications and adaptive evolution of avian apparatus of bipedal locomotion*. Moscow: KMK Scientific Press Ltd.

II.9 Figure captions

Figure 1. The musculoskeletal model of the chicken hindlimb developed in this study. This is shown in the 'neutral posture' for all joints, that is, when all joint angles are zero. (A–C) Geometries of the musculotendon actuators in relation to the bones, in lateral (A), anterior (B) and oblique anterolateral (C) views. (D–F) Location and orientation of joint coordinate systems (red, green and blue axes), the centres of mass for each segment (grey and white balls) and the soft tissue volumes, derived from CT scans and used to calculate mass properties; these are shown in the same views as A–C. Also reported in F are the masses for each segment. In D–F, the flexion-extension axis of each joint is the blue axis. For scale, the length of each arrow in the triad of the global coordinate system is 40 mm.

Figure 2. Musculoskeletal simulation of a given test posture. Muscles that are active are red, whilst those set to be inactive during simulation are blue. External loads applied to the pes segment are the vertical ground reaction force (GRF) and moments about the *x* and *y* axes (M_x and M_y, respectively). A reserve actuator is also applied to the metatarsophalangeal joint (purple). Loads are not shown to scale.

Figure 3. Finite element simulation of a given test posture. (A, B) For each posture, two simulations were performed, one for the femur (A) and one for the tibiotarsus + fibula (B). Muscle and ligament forces are red, segment weights are blue, joint forces are green and joint moments are orange. The focal bones in each simulation were 'bookended' between their adjacent articulating bones, to which restraints or joint forces were applied. (C) The intervening soft tissues between focal bones and their neighbouring bones were modelled as a single homogenous volume (turquoise). (D) Knee joint forces were applied as a remote force: the force was applied to a remote point (knee joint centre, red dot), which was topologically attached to a neighbouring bone via constraint equations (red lines, schematic illustration only). Loads are not shown to scale.

Figure 4. The identified solution posture for the chicken. (A) Calculated angular deviation between $\boldsymbol{\sigma}_3$ and $\mathbf{u}_1$ in the femoral head (grey bars) and medial femoral condyle (white bars) for each posture tested, with the last (8^{th}) posture identified as the 'solution'. This shows the progressive improvement in alignment between principal stresses and cancellous bone architecture across the postures tested. (B–D) The solution posture in lateral (B), dorsal (C) and anterior (D) views; also illustrated in B are stick figure representations of the other postures tested, and the whole-body COM of the solution posture. The solution posture resulted in the greatest degree of overall correspondence between principal stress trajectories and observed cancellous bone architectural patterns in birds, as assessed by qualitative comparisons across the femur, tibiotarsus and fibula, as well as quantitative results for the femoral head and medial femoral condyle.

Figure 5. Principal stress trajectories for the femur in the solution posture. For easier visual comparison, these stress trajectories were 'downsampled' in a custom MATLAB script, by interpolating the raw stress results at each finite element node to a regular grid. (A, B) Vector field of $\boldsymbol{\sigma}_3$ in the femoral head, plotted on a translucent rendering of the external bone geometry, in anterior (A) and medial (B) views. (C, D) Vector field of $\boldsymbol{\sigma}_3$ in the region under the facies antitrochanterica, in anterior (C) and lateral (D) views. (E, F) Vector field of $\boldsymbol{\sigma}_3$ in the trochanteric crest, in anterior (E) and lateral (F) views. (G) Vector field of $\boldsymbol{\sigma}_3$ in a 3-D slice through the medial femoral condyle, parallel to the sagittal plane and in medial view. (H) Vector field of $\boldsymbol{\sigma}_3$ in a 3-D slice through the lateral femoral condyle, parallel to the sagittal plane and in lateral view. Compare the stress trajectories in A–H with the fabric vector fields illustrated in Figs 16 and 24 of Part I. (I) Comparison of the mean direction of $\boldsymbol{\sigma}_3$ in the femoral head and the mean direction of $\mathbf{u}_1$ for birds, plotted on an equal-angle stereoplot, with northern hemisphere projection (using StereoNet 9.5; Allmendinger et al. 2013; Cardozo & Allmendinger 2013). (J) Comparison of the mean direction of $\boldsymbol{\sigma}_3$ in the medial femoral condyle and the mean direction of $\mathbf{u}_1$ for birds, plotted on an equal-angle stereoplot, with southern hemisphere projection. Insets in I and J show locations of regions for which the mean direction of $\boldsymbol{\sigma}_3$ was calculated. The orange dots in I and J indicate the mean direction of $\boldsymbol{\sigma}_3$ for the muscle force sensitivity test; note how close these are to the original results (blue).

Figure 6. Principal stress trajectories for the tibiotarsus in the solution posture. (A, B) Vector field of $\boldsymbol{\sigma}_1$ in the anterior cnemial crest, in anterior (A) and medial (B) views. (C, D) Vector field of $\boldsymbol{\sigma}_1$ in the anterior cnemial crest in the muscle force sensitivity test, shown in the same views as A and B, respectively. (E, F) Vector field of $\boldsymbol{\sigma}_3$ in the lateral cnemial crest, in anterior (E) and lateral (F) views. (G, H) Vector field of $\boldsymbol{\sigma}_3$ under the medial articular facies, shown as 3-D slices parallel to the coronal plane (G, posterior view) and sagittal plane (H, medial view). (I, J) Vector field of $\boldsymbol{\sigma}_3$ under the lateral articular facies, shown as 3-D slices parallel to the coronal plane (I, posterior view) and sagittal plane (J, lateral view). (K) Vector field of $\boldsymbol{\sigma}_1$ (red) and $\boldsymbol{\sigma}_3$ (blue) in a 3-D slice through the middle of the proximal metaphysis, parallel to the sagittal plane. Schematic

inset shows the double-arcuate pattern formed by the two stress trajectories. (L, M) Vector field of $\boldsymbol{\sigma}_3$ in the articular condyles (purple = lateral condyle, pink = medial condyle) of the distal tibiotarsus, shown for 3-D slices through the middle of the condyles, in oblique anterolateral (L) and anteromedial (M) views. Compare the stress trajectories illustrated here with the fabric vector fields illustrated in Figs 31 and 36 of Part I.

Figure 7. Principal stress trajectories for the fibula in the solution posture. (A) Vector field of $\boldsymbol{\sigma}_1$ in the medial side of the fibular head, in medial view (reversed). (B) Vector field of $\boldsymbol{\sigma}_3$ in lateral side of the fibular head, in lateral view. Compare the stress trajectories here with the vector fields and isosurfaces illustrated in Fig. 40G–K of Part I.

Figure 8. Additional aspects of the solution posture. (A) The trajectories $\boldsymbol{\sigma}_1$ (red) and $\boldsymbol{\sigma}_3$ (blue) at the femoral mid-shaft, in anterior view. (B) The oblique nature of the principal stresses in the femoral mid-shaft is indicative of strong torsional loading, with a positive sense. (C) The trajectories of $\boldsymbol{\sigma}_1$ and $\boldsymbol{\sigma}_3$ at the tibial mid-shaft, in anterior view. (D) Activations for each muscle actuator in the musculoskeletal simulation. (E) Flexion-extension muscle moment arms for the hip, knee and ankle joints; positive values indicate extension, negative values indicate flexion. For keys to abbreviations in D and E, see Table 1.

Table 1(on next page)

The origins and insertions of each of the muscles and ligamentsrepresented in the chicken musculoskeletal model.

Those muscles that attach to the patella or patellar tendon were modelled as attaching in a general fashion to the apices of one of the cnemial crests (identified in brackets).

Table 1. The origins and insertions of each of the muscles and ligaments represented in the chicken musculoskeletal model. Those muscles that attach to the patella or patellar tendon were modelled as attaching in a general fashion to the apices of one of the cnemial crests (identified in brackets).

Muscle or ligament	Abbreviation	Origin	Insertion
Iliotibialis cranialis	IC	Anterior rim of dorsal iliac crest	Patellar tendon [medial aspect of anterior cnemial crest]
Iliotibialis lateralis pars preacetabularis	ILPR	Dorsolateral iliac crest, anterior to acetabulum	Patellar tendon [anterior cnemial crest]
Iliotibialis lateralis pars postacetabularis	ILPO	Dorsolateral iliac crest, posterior to acetabulum	Patellar tendon [anterior cnemial crest]
Ambiens	AMB	Preacetabular process on proximal pubis	Lateral fibular head
Femorotibialis externus	FMTE	Lateral femoral shaft	Patellar tendon [anterior cnemial crest]
Femorotibialis medius	FMTM	Anterior femoral shaft	Patellar tendon [anterior cnemial crest]
Femorotibialis internus	FMTI	Medial femoral shaft	Patellar tendon [medial aspect of anterior cnemial crest]
Iliofibularis	ILFB	Lateral postacetabular ilium, anterior to FCLP	Fibular tubercle
Flexor cruris lateralis pars pelvica	FCLP	Lateral surface of posterior end of ilium and adjacent caudal vertebrae	Medial proximal tibiotarsus
Flexor cruris lateralis pars accessoria	FCLA	From FCLP	Distal posterior femur
Flexor cruris medialis	FCM	Lateral surface of posterior end of ischium	Medial proximal tibiotarsus
Iliofemoralis externus	IFE	Processus supratrochantericus of ilium	Trochanteric shelf of femur
Iliofemoralis internus	IFI	Ventral preacetabular ilium, ventral to ITM	Medial surface of proximal femur (distal to femoral head)
Iliotrochantericus cranialis	ITCR	Ventral preacetabular ilium, posterior to ITCR	Anterolateral surface of femoral trochanter
Iliotrochantericus medius	ITM	Ventral preacetabular ilium	Anterolateral surface of femoral trochanter, distal to ITC
Iliotrochantericus caudalis	ITC	Lateral surface of preacetabular ilium	Anterolateral surface of femoral trochanter, distal to ITC
Ischiofemoralis	ISF	Lateral ischium	Lateral proximal femur
Caudofemoralis pars caudalis	CFC	Ventrolateral surface of pygostyle	Posterior surface of proximal femoral shaft
Caudofemoralis pars pelvica	CFP	Lateral ilium, posterior to ILFB and dorsal to ISF	Posterior surface of proximal femoral shaft (lateral to CFC)
Obturatorius medialis	OM	Medial surfaces of ischium and pubis	Posterolateral surface of proximal femur

Table 1 (continued).

Muscle or ligament	Abbreviation	Origin	Insertion
Puboischiofemoralis pars lateralis	PIFL	Ventral ischium and pubis	Posterior surface of femoral shaft, lateral to PIFM
Puboischiofemoralis pars medialis	PIFM	Ventral ischium and pubis (ventral to PIFL)	Posterior surface of femoral shaft, medial to PIFL
Gastrocnemius lateralis	GL	Lateral aspect of distal femur (proximal to lateral condyle)	Posterior surface of tarsometatarsus
Gastrocnemius intermedia	GI	Medial aspect of distal femur (near medial condyle)	Posterior surface of tarsometatarsus
Gastrocnemius medialis	GM	Anteromedial proximal tibiotarsus	Posterior surface of tarsometatarsus
Flexor digitorum longus	FDL	Caudal surface of tibiotarsus	Ventral aspect of digit II-IV phalanges
Other digital flexors*	ODF	Caudal femur, near lateral condyle (but proximal to it)	Ventral aspect of digit II-IV phalanges
Flexor hallucis longus	FHL	Caudal distal femur, popliteal fossa region	Ventral aspect of phalanx II-2 (ungual)
Extensor digitorum longus	EDL	Anterior surface of tibiotarsus, distal to TCT origin	Dorsal aspect of digit II-IV phalanges; passes under pons supratendinous
Other digital extensors**	ODE	Anterior aspect of tarsometatarsus	Dorsal aspect of digit II-IV phalanges
Tibialis cranialis caput femorale	TCF	Distal lateral condyle of femur	Anterior proximal tarsometarsus
Tibialis cranialis caput tibiale	TCT	Distal aspect of anterior cnemial crest	Anterior proximal tarsometarsus
Fibularis longus	FL	Soft tissues surounding proximolateral tibiotarsus [apex of lateral cnemial crest]	Tendon of flexor perforati digiti III [modelled separately, to insert on ventral pes]
Fibularis brevis	FB	Craniolateral tibiotarsus and craniomedial fibula	Lateral proximal tarsometatarsus
Knee medial collateral ligament	KMCL	Depression on medial surface of medial femoral condyle	Medial proximal tibiotarsus, proximal to FCLP and FCM insertions
Knee lateral collateral ligament	KLCL	Depression on lateral surface of lateral femoral condyle	Lateral fibular head, proximal to AMB insertion
Ankle medial collateral ligament	AMCL	Depression on medial surface of medial condyle of tibiotarsus	Medial proximal tarsometatarsus
Ankle lateral collateral ligament	ALCL	Depression on lateral surface of lateral condyle of tibiotarsus	Lateral proximal tarsometatarsus, anterior to FB insertion

*ODF includes the flexores perforantes et perforatus digitorum II et III and flexores perforatus digitorum II, III et IV.
**ODE includes the extensores brevis digitorum III et IV and extensor proprius digiti III.

Table 2(on next page)

Assumed activities of the muscle actuators used in the simulations.

X = active (capable of exerting up to 30.597 N of force), O = inactive (exerts zero force).

Table 2. Assumed activities of the muscle actuators used in the simulations. X = active (capable of exerting up to 30.597 N of force), O = inactive (exerts zero force).

Muscle	Activity
IC	O
ILPR	O
ILPO	X
AMB	X
FMTE	X
FMTM	X
FMTI	X
ILFB	X
FCLP	X
FCLA	X
FCM	X
IFE	O
IFI	O
ITCR	O
ITM	X
ITC	X
ISF	X
CFC	X
CFP	X
OM	O
PIFL	X
PIFM	X
GL	X
GI	X
GM	X
FDL	X
ODF	X
FHL	X
EDL	O
ODE	O
TCF	O
TCT	O
FL	X
FB	X

Table 3(on next page)

Material properties used in the finite element analysis component of thesimulations.

All entities were modelled as solid, isotropic, linearly elastic materials.

Table 3. Material properties used in the finite element analysis component of the simulations. All entities were modelled as solid, isotropic, linearly elastic materials.

Material	Density (kg/m^3)	Young's modulus (MPa)	Poisson's ratio
Bone	2,060	17,000	0.3
Cartilage	1,100	50	0.45
Knee soft tissues*	1,100	100	0.3

*The knee soft tissues material properties reflected a composite of those of both cartilage and menisci.

Table 4(on next page)

Maximum force capability of the active muscle actuators used in themuscle force sensitivity test.

Note how the force capability can vary widely, from less than 0.1 BW (AMB) to over 6 BW (FMTI).

Table 4. Maximum force capability of the active muscle actuators used in the muscle force sensitivity test. Note how the force capability can vary widely, from less than 0.1 BW (AMB) to over 6 BW (FMTI).

Muscle	F_{max} (N)
ILPO	30.111
AMB	1.112
FMTE	19.636
FMTM	21.007
FMTI	92.110
ILFB	24.777
FCLP	20.760
FCLA	18.656
FCM	8.713
ITM	3.003
ITC	77.382
ISF	25.635
CFC	1.625
CFP	6.300
PIFL	7.981
PIFM	17.940
GL	59.539
GI	10.863
GM	71.969
FDL	31.022
ODF	58.122
FHL	22.672
FL	51.621
FB	8.737

Figure 1(on next page)

The musculoskeletal model of the chicken hindlimbdeveloped in this study.

This is shown in the ‘neutral posture’ for all joints, that is, when all joint angles are zero. (A–C) Geometries of the musculotendon actuators in relation to the bones, in lateral (A), anterior (B) and oblique anterolateral (C) views. (D–F) Location and orientation of joint coordinate systems (red, green and blue axes), the centres of mass for each segment (grey and white balls) and the soft tissue volumes, derived from CT scans and used to calculate mass properties; these are shown in the same views as A–C. Also reported in F are the masses for each segment. In D–F, the flexion-extension axis of each joint is the blue axis. For scale, the length of each arrow in the triad of the global coordinate system is 40 mm.

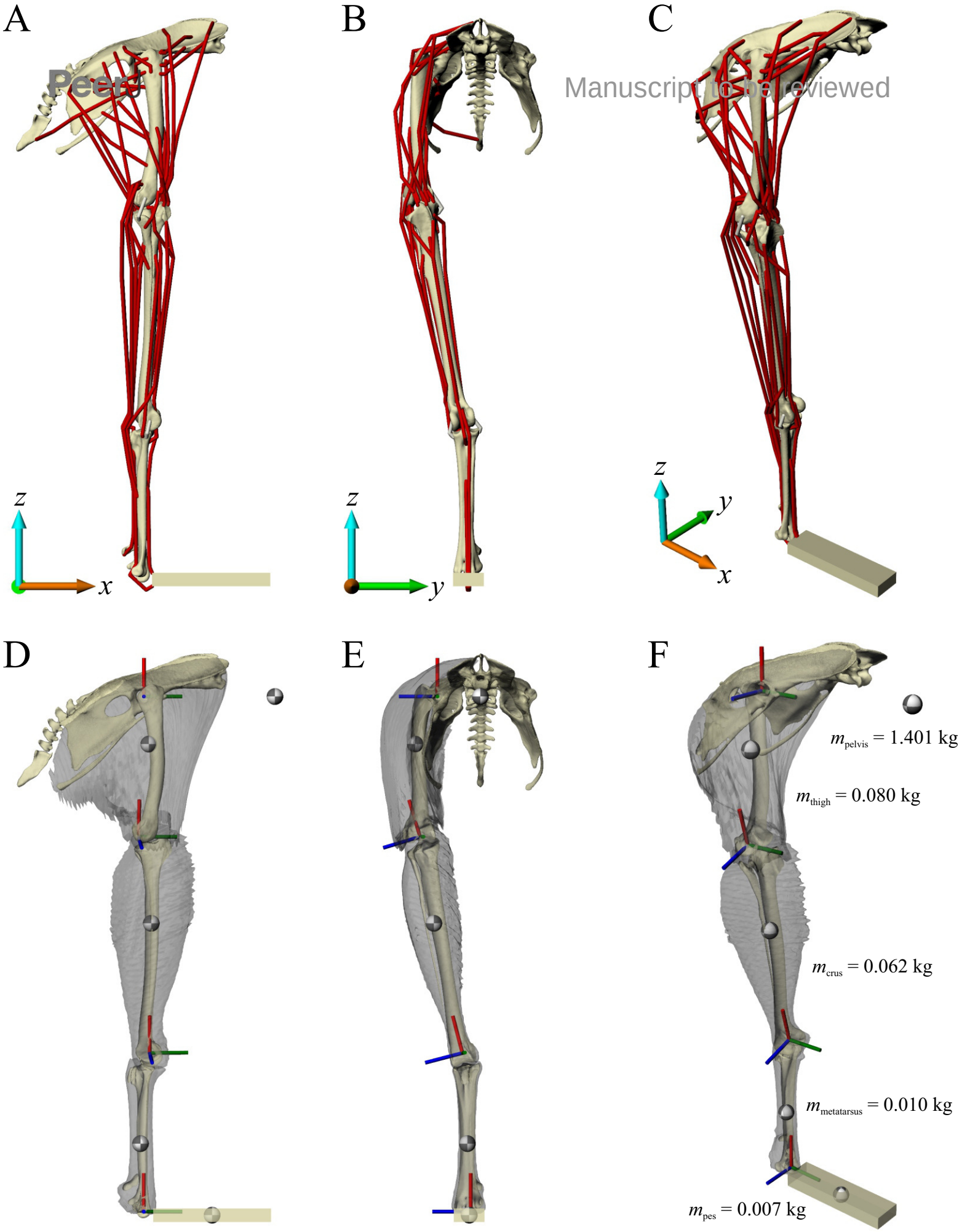

Figure 2(on next page)

Musculoskeletal simulation of a given test posture.

Muscles that are active are red, whilst those set to be inactive during simulation are blue. External loads applied to the pes segment are the vertical ground reaction force (GRF) and moments about the x and y axes (M_x and M_y, respectively). A reserve actuator is also applied to the metatarsophalangeal joint (purple). Loads are not shown to scale.

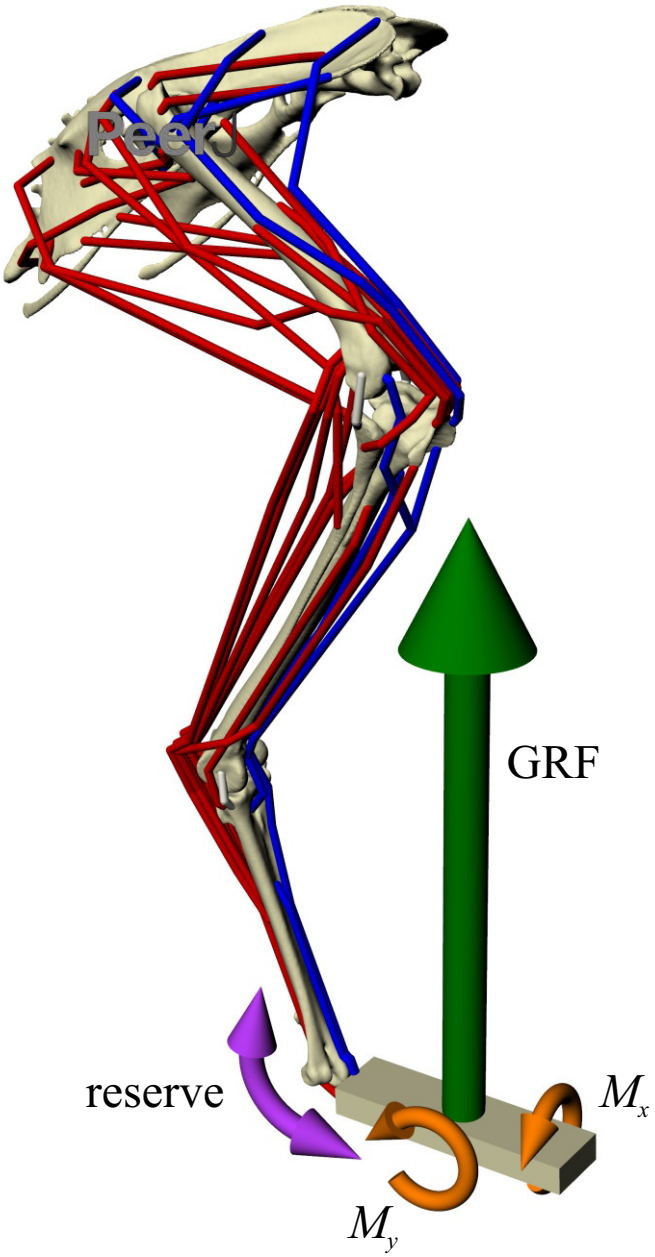
GRF
reserve
M_x
M_y

Figure 3(on next page)

Finite element simulation of a given test posture.

(A, B) For each posture, two simulations were performed, one for the femur (A) and one for the tibiotarsus + fibula (B). Muscle and ligament forces are red, segment weights are blue, joint forces are green and joint moments are orange. The focal bones in each simulation were 'bookended' between their adjacent articulating bones, to which restraints or joint forces were applied. (C) The intervening soft tissues between focal bones and their neighbouring bones were modelled as a single homogenous volume (turquoise). (D) Knee joint forces were applied as a remote force: the force was applied to a remote point (knee joint centre, red dot), which was topologically attached to a neighbouring bone via constraint equations (red lines, schematic illustration only). Loads are not shown to scale.

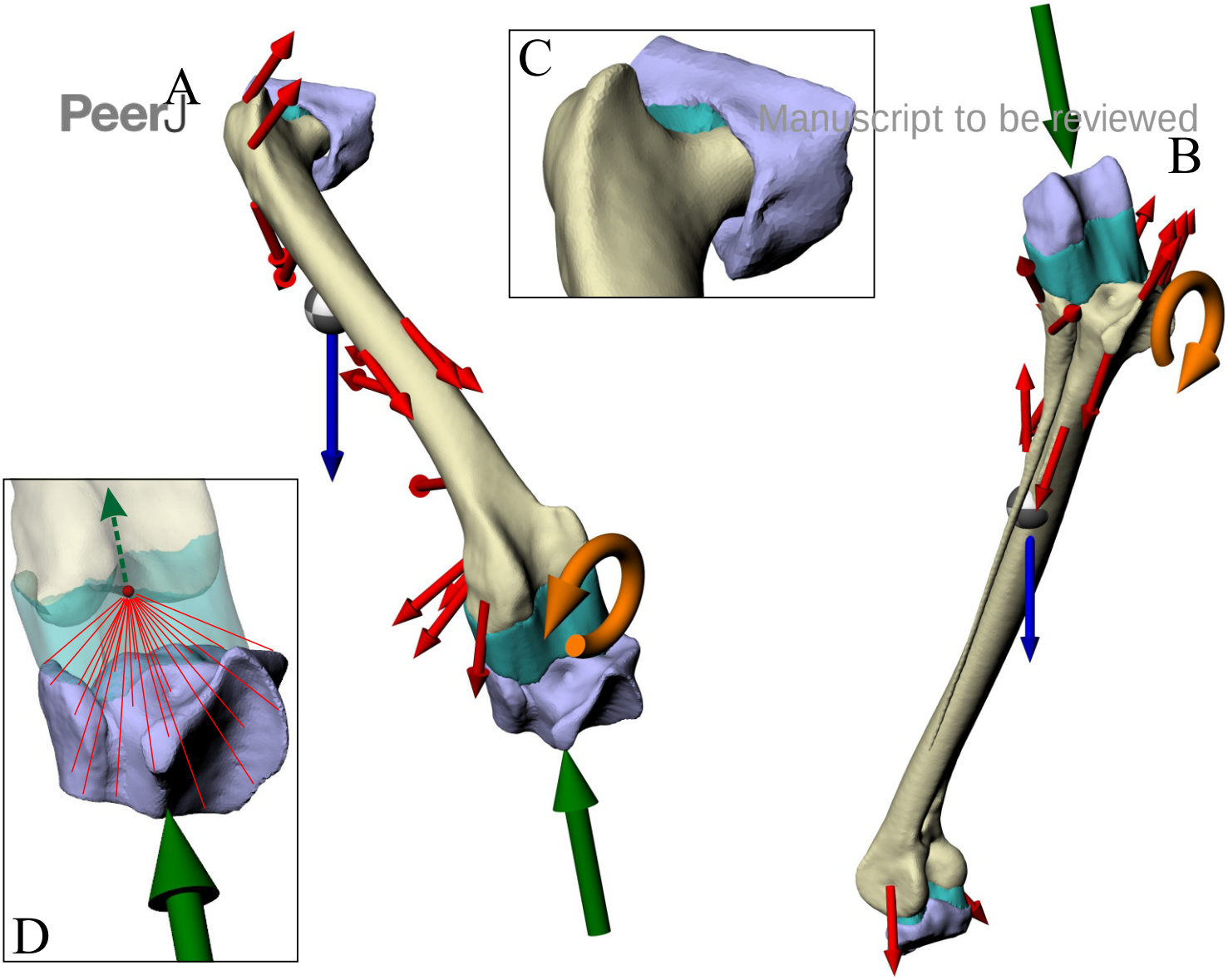

Figure 4(on next page)

The identified solution posture for the chicken.

(A) Calculated angular deviation between $\boldsymbol{\sigma}_3$ and $\mathbf{u}_1$ in the femoral head (grey bars) and medial femoral condyle (white bars) for each posture tested, with the last (8^{th}) posture identified as the 'solution'. This shows the progressive improvement in alignment between principal stresses and cancellous bone architecture across the postures tested. (B–D) The solution posture in lateral (B), dorsal (C) and anterior (D) views; also illustrated in B are stick figure representations of the other postures tested, and the whole-body COM of the solution posture. The solution posture resulted in the greatest degree of overall correspondence between principal stress trajectories and observed cancellous bone architectural patterns in birds, as assessed by qualitative comparisons across the femur, tibiotarsus and fibula, as well as quantitative results for the femoral head and medial femoral condyle.

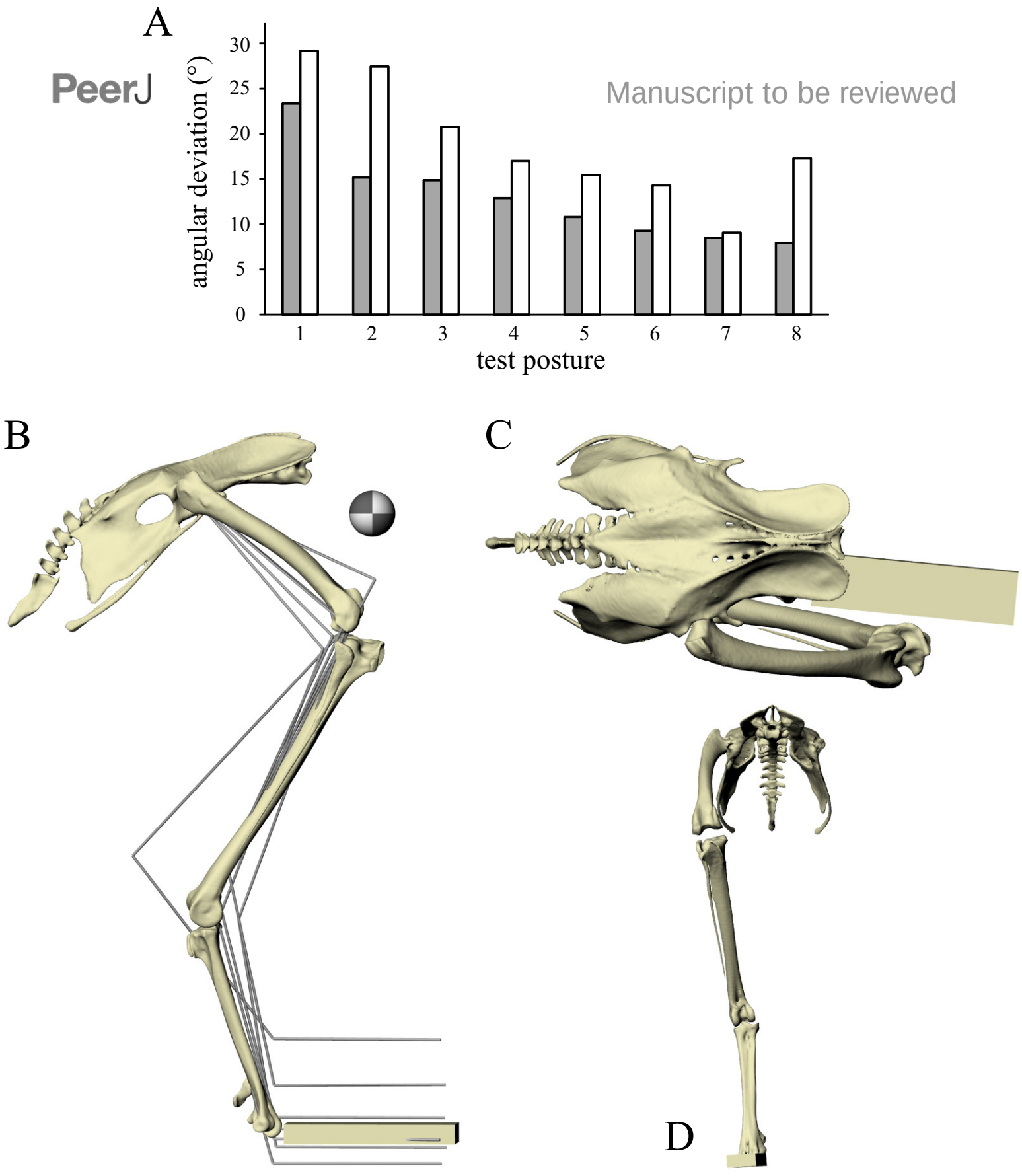
A
angular deviation (°)
30
25
20
15
10
5
0
1
2
3
4
5
6
7
8
test posture
B
C
D

Figure 5(on next page)

Principal stress trajectories for the femur in thesolution posture.

For easier visual comparison, these stress trajectories were ‘downsampled’ in a custom MATLAB script, by interpolating the raw stress results at each finite element node to a regular grid. (A, B) Vector field of $\boldsymbol{\sigma}_3$ in the femoral head, plotted on a translucent rendering of the external bone geometry, in anterior (A) and medial (B) views. (C, D) Vector field of $\boldsymbol{\sigma}_3$ in the region under the facies antitrochanterica, in anterior (C) and lateral (D) views. (E, F) Vector field of $\boldsymbol{\sigma}_3$ in the trochanteric crest, in anterior (E) and lateral (F) views. (G) Vector field of $\boldsymbol{\sigma}_3$ in a 3-D slice through the medial femoral condyle, parallel to the sagittal plane and in medial view. (H) Vector field of $\boldsymbol{\sigma}_3$ in a 3-D slice through the lateral femoral condyle, parallel to the sagittal plane and in lateral view. Compare the stress trajectories in A–H with the fabric vector fields illustrated in Figs 16 and 24 of Part I. (I) C omparison of the mean direction of $\boldsymbol{\sigma}_3$ in the femoral head and the mean direction of $\mathbf{u}_1$ for birds, plotted on an equal-angle stereoplot, with northern hemisphere projection (using StereoNet 9.5; Allmendinger et al. 2013; Cardozo & Allmendinger 2013) . (J) C omparison of the mean direction of $\boldsymbol{\sigma}_3$ in the medial femoral condyle and the mean direction of $\mathbf{u}_1$ for birds, plotted on an equal-angle stereoplot, with southern hemisphere projection. Insets in I and J show locations of regions for which the mean direction of $\boldsymbol{\sigma}_3$ was calculated. The orange dots in I and J indicate the mean direction of $\boldsymbol{\sigma}_3$ for the muscle force sensitivity test; note how close these are to the original results (blue).

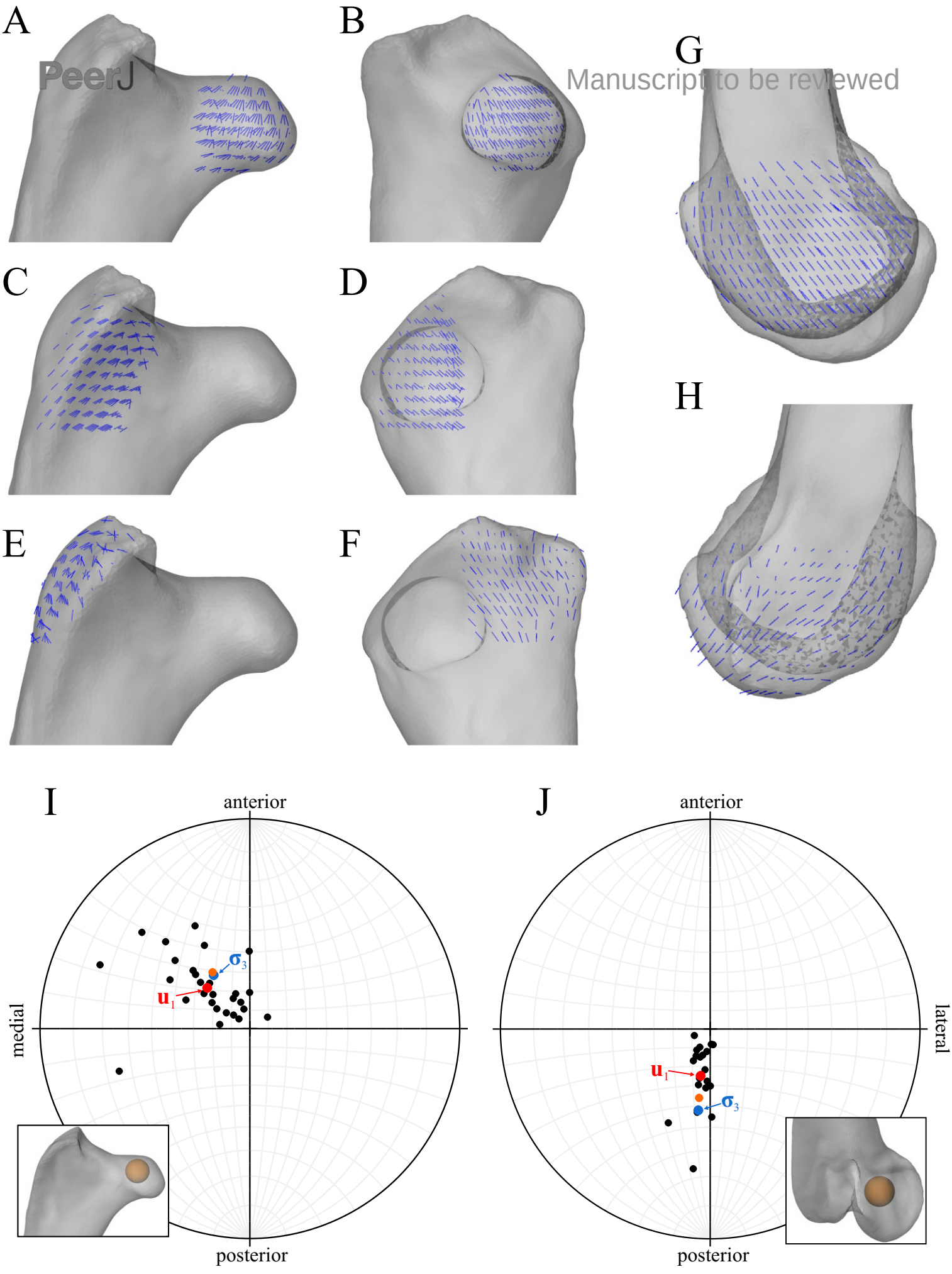

Figure 6(on next page)

Principal stress trajectories for the tibiotarsus inthe solution posture.

(A, B) Vector field of $\boldsymbol{\sigma}_1$ in the anterior cnemial crest, in anterior (A) and medial (B) views. (C, D) Vector field of $\boldsymbol{\sigma}_1$ in the anterior cnemial crest in the muscle force sensitivity test, shown in the same views as A and B, respectively. (E, F) Vector field of $\boldsymbol{\sigma}_3$ in the lateral cnemial crest, in anterior (E) and lateral (F) views. (G, H) Vector field of $\boldsymbol{\sigma}_3$ under the medial articular facies, shown as 3-D slices parallel to the coronal plane (G, posterior view) and sagittal plane (H, medial view). (I, J) Vector field of $\boldsymbol{\sigma}_3$ under the lateral articular facies, shown as 3-D slices parallel to the coronal plane (I, posterior view) and sagittal plane (J, lateral view). (K) Vector field of $\boldsymbol{\sigma}_1$ (red) and $\boldsymbol{\sigma}_3$ (blue) in a 3-D slice through the middle of the proximal metaphysis, parallel to the sagittal plane. Schematic inset shows the double-arcuate pattern formed by the two stress trajectories. (L, M) Vector field of $\boldsymbol{\sigma}_3$ in the articular condyles (purple = lateral condyle, pink = medial condyle) of the distal tibiotarsus, shown for 3-D slices through the middle of the condyles, in oblique anterolateral (L) and anteromedial (M) views. Compare the stress trajectories illustrated here with the fabric vector fields illustrated in Figs 31 and 36 of Part I.

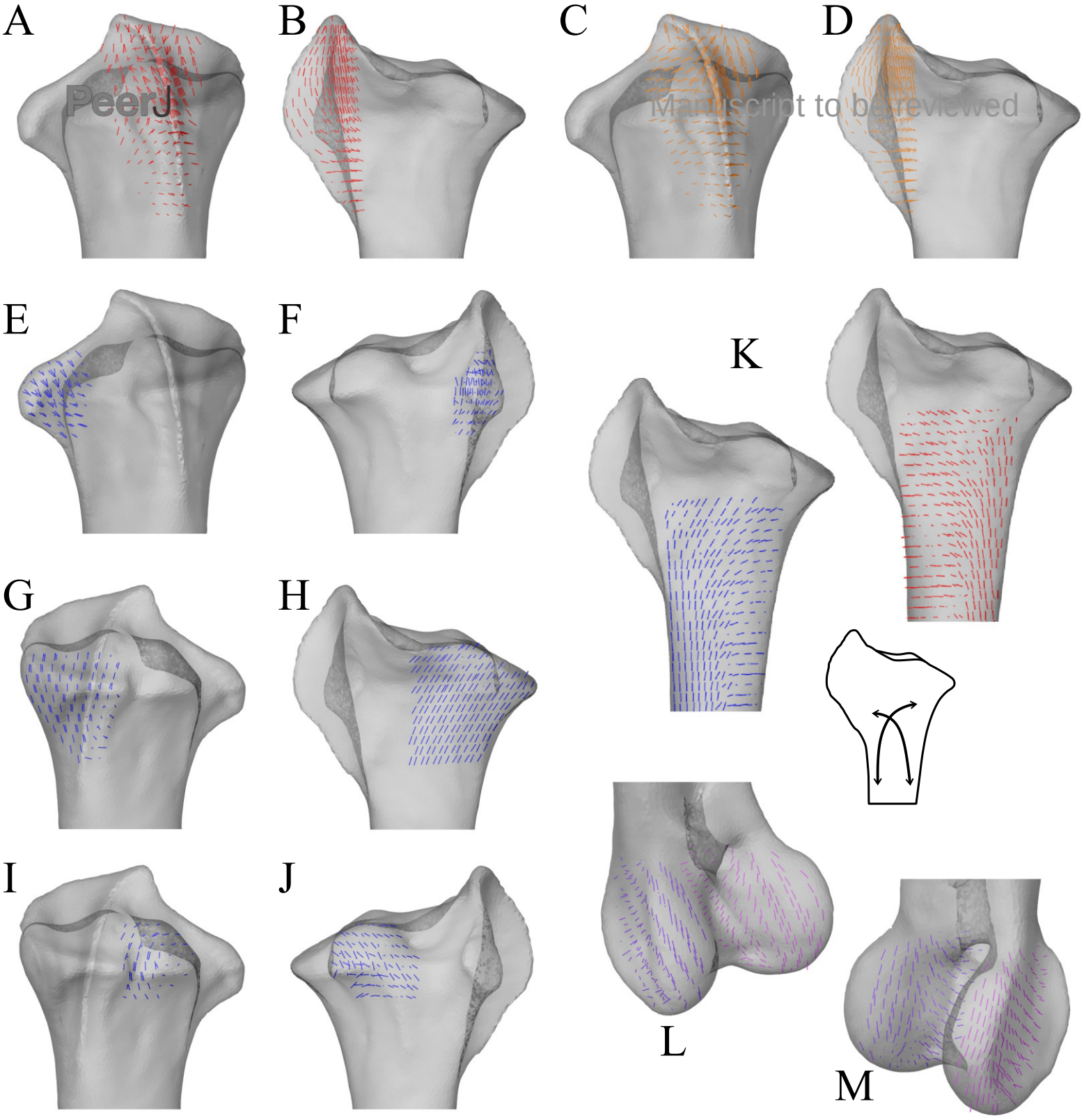

Figure 7 (on next page)

Principal stress trajectories for the fibula in the solution posture.

(A) Vector field of $\boldsymbol{\sigma}_1$ in the medial side of the fibular head, in medial view (reversed). (B) Vector field of $\boldsymbol{\sigma}_3$ in lateral side of the fibular head, in lateral view. Compare the stress trajectories here with the vector fields and isosurfaces illustrated in Fig. 40G–K of Part I.

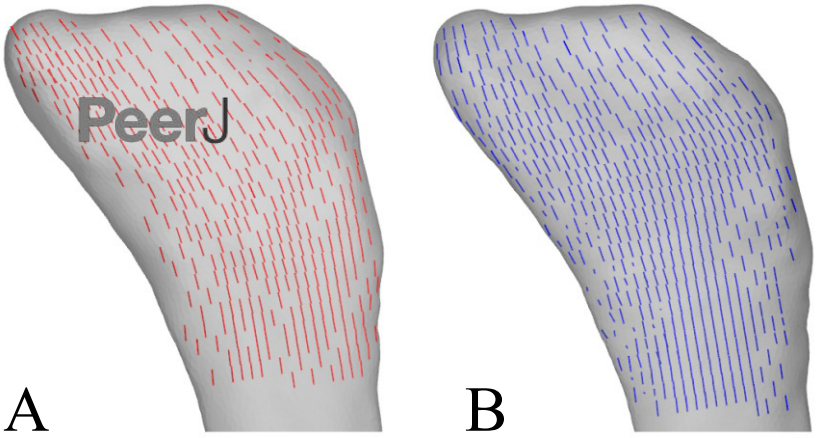

Figure 8(on next page)

Additional aspects of the solution posture.

(A) The trajectories $\boldsymbol{\sigma}_1$ (red) and $\boldsymbol{\sigma}_3$ (blue) at the femoral mid-shaft, in anterior view. (B) The oblique nature of the principal stresses in the femoral mid-shaft is indicative of strong torsional loading, with a positive sense. (C) The trajectories of $\boldsymbol{\sigma}_1$ and $\boldsymbol{\sigma}_3$ at the tibial mid-shaft, in anterior view. (D) Activations for each muscle actuator in the musculoskeletal simulation. (E) Flexion-extension muscle moment arms for the hip, knee and ankle joints; positive values indicate extension, negative values indicate flexion. For keys to abbreviations in D and E, see Table 1.

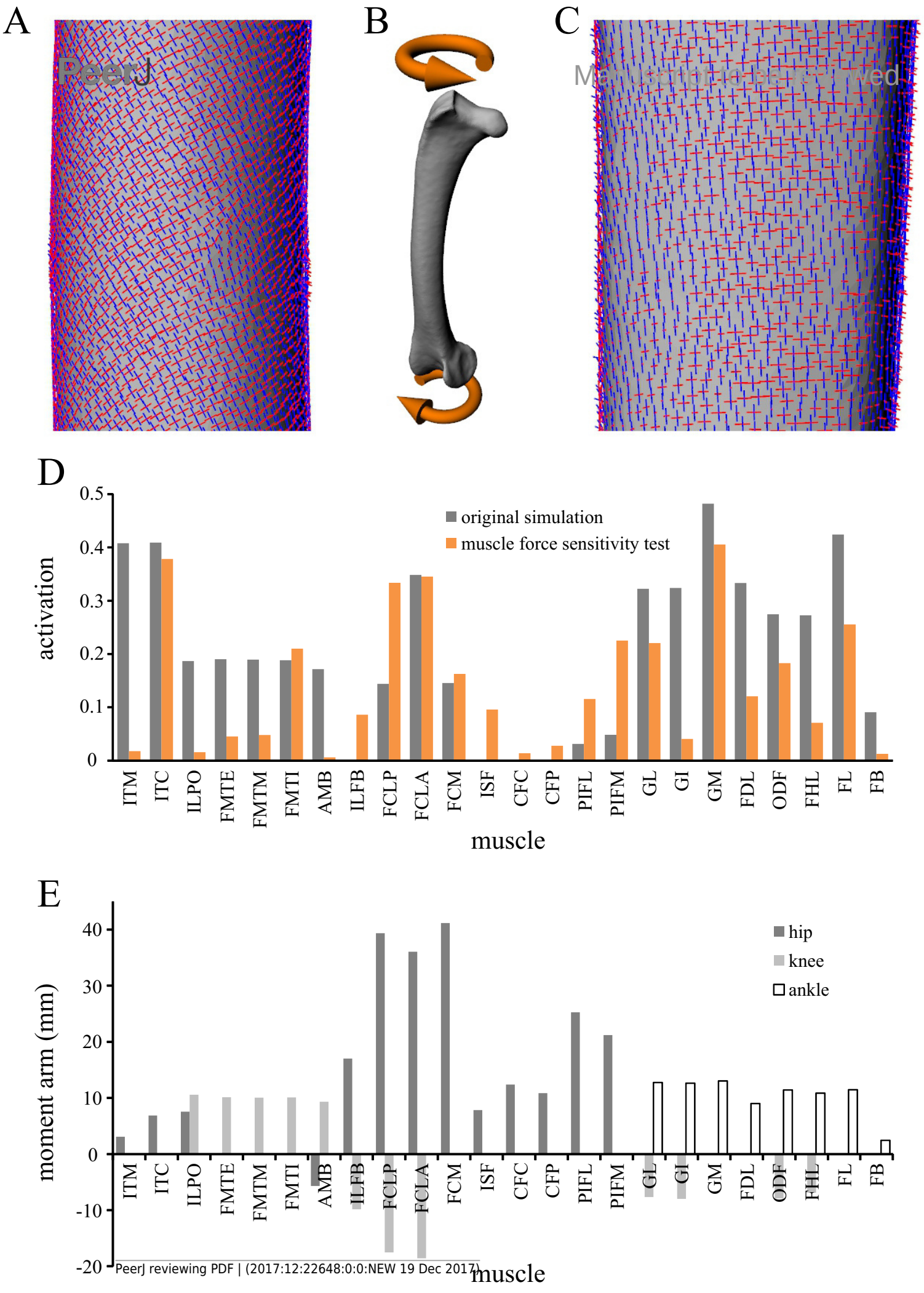
A
B
C
D
original simulation
muscle force sensitivity test
activation
0.5
0.4
0.3
0.2
0.1
0
ITM
ITC
ILPO
FMTE
FMTM
FMTI
AMB
ILFB
FCLP
FCLA
FCM
ISF
CFC
CFP
PIFL
PIFM
GL
GI
GM
FDL
ODF
FHL
FL
FB
muscle
E
hip
knee
ankle
moment arm (mm)
40
30
20
10
0
-10
-20
muscle